The Mechanical Behaviour of Panzhihua Iron Tailings

W. Li[1*] and M. R. Coop[2]

[1] Department of Architecture and Civil Engineering, City University of Hong Kong, Hong Kong

[2] University College London, UK; formerly City University of Hong Kong, Hong Kong

[*] Corresponding author

ABSTRACT

Safety problems have concerned many researchers studying tailings dam in recent years, since they have a high risk of failure due to liquefaction. Existing analysis of liquefaction in tailings within a critical state framework have relied on the critical state line (CSL) being unique in the volumetric plane. However, recent advances have highlighted a so-called "transitional" behaviour in which the location of the normal compression line (NCL) and CSL is a function of the density of the soils at deposition. This paper presents a detailed investigation of the mechanics of tailings taken from three locations of an iron tailings impoundment. Reconstituted samples were prepared by different methods and at different densities. No transitional behaviour was found, although the results show that the rate of convergence of the compression curves changes, with the finest pond material reaching a unique NCL earliest. The preparation method was found not to have a large effect on the behaviour for these tailings. Unique CSL could be clearly identified for all the three tailings but with different shapes, giving rise to a changing susceptibility to liquefaction. This susceptibility tends to increase from the pond to the upper beach.

KEYWORDS: tailings; critical state; transitional behaviour; fabric; liquefaction.

INTRODUCTION

Tailings are the residual materials after extracting valuable minerals from ores. The characteristics of tailings are highly variable depending on the composition of the ores and the extraction processes used. There are several suitable methods to dispose of different kinds of tailings, including tailings dams, paste tailings, dry stacking, underground backfilling, open-pit backfilling and subaqueous disposal (Vick 1983), among which tailings dams are the most common method. The iron tailings impoundment, as shown in Figure 1, in Panzhihua city, Sichuan, China, is one of the largest tailings dams in Asia. It was constructed using the upstream method from 1966 to 1970, with a maximum height of 210 m and a capacity of 186 million m^3. For such a high tailings dam, stability is the main concern.

Due to the small particle size and high water contents, tailings materials often have a high risk of failure. There were more than 240 tailings dam incidents between 1917 and 2014 (ICOLD 2002; WISE 2014). In China, the most deadly recent tailings dam failure was in 2008 in Xiangfen County, Shanxi Province, which caused the deaths of 277 people (WISE 2014). Among the various failures, unusually heavy rain is the most common cause of tailings dam failures, and the second cause is liquefaction under either static or seismic loading. Often liquefaction may exacerbate an initial failure. For example, Fourie et al. (2001) identified that an overtopping at the Merriespruit gold tailings dam in South Africa may have led to a static liquefaction that killed 17 people. At the Aznalcóllar dam failure in 1998 in Spain it was an initial foundation failure that led to the static liquefaction and release of 4-5 million m^3 of slurry and fluids (Davies and Lighthall 2001). In Italy in 1985 the Stava tailings dam initially failed through inadequate design of the dams, and the resulting debris flow reached 90km/h killing 268 people (Chandler and Tosatti 1995). Carrera et al. (2011) discussed the failure from the mechanical behaviour of the Stava tailings with different fines contents and suggested that the embankment material was the most susceptible to liquefaction.

However, their investigation was limited to creating artificial gradings by mixing coarse and fine fractions, and as will be discussed later, such artificially graded mixtures may not simulate well the behaviour of the actual gradings around tailings structures.

For the analysis of liquefaction, intensive research has been done within a critical state framework. The state parameter proposed by Been and Jefferies (1985) has been widely used to assess the susceptibility to liquefaction. It was pointed out that soils lying on the wet side of the CSL, with positive state parameters, were more prone to get liquefied (e.g. Yang 2002). However, the CSL for sand often tends to be curved or bi-linear (e.g. Been et al. 1991; Verdugo and Ishihara 1996) at low stress levels, which may create problems in applying the state parameter and Bobei et al. (2009) pointed out that, for a curved CSL, a positive state parameter necessarily gave true liquefaction at low stress levels, whereas the same positive state parameter at high stresses would not give liquefaction. A modified state parameter was therefore proposed which could capture this so called "reverse" behaviour (Yamamuro and Lade 1998) which indicated that the stability of the silty sands increased with an increasing confining stress. Similar patterns of behaviour were found by Carrera et al. (2011) and Bedin et al. (2012) in their studies of liquefaction of tailings. They identified that the curved CSL gave rise to a changing susceptibility to liquefaction as the stress level increased. Generally the curvature of a CSL is caused by the onset of the particle breakage (Konrad 1998), which was also identified in the gold tailings tested by Bedin et al. (2012). However, for the Stava tailings tested by Carrera et al. (2011), no particle breakage was found. Fourie and Tshabalala (2005) carried out monotonic undrained triaxial compression tests on gold tailings under both isotropic and K_0 consolidation conditions and found the significant effect of K_0 consolidation in identifying the stresses correctly that will trigger liquefaction.

Recent advances have highlighted that many soils have a so-called "transitional" behaviour (e.g. Martins et al. 2001; Nocilla et al. 2006; Shipton and Coop 2012), in which samples of

initially different densities have non-unique NCLs in compression and non-unique CSLs in shear, resulting in difficulty to characterise soil behaviour under the critical state framework. Some recent research has shown that transitional behaviour can also be found in particular types of tailings. Tan (2004; reported in Coop 2015) analysed commercial test data for Stava tailings and showed that silty tailings taken from different depths but with similar grading did not have a unique NCL. However, Carrera et al. (2011) conducted tests on the same tailings but with different gradings and found no transitional behaviour. Al-Tarhouni et al. (2011) carried out simple shear tests on gold tailings and reported that the final states were dependent on the initial density with no unique relationship between the shear strength and the current void ratio, which might arise from transitional behaviour. Coop (2015) also reported transitional behaviour in a number of other tailings.

There is also some debate about whether the initial fabric from sample preparation has a significant effect on the behaviour of soils, like susceptibility to liquefaction. Ishihara (1993) and Zlatovic and Ishihara (1997) reported that the undrained behaviours of Nevada and Toyoura sands were affected markedly by different preparation methods, giving strain hardening behaviour for water pluviated samples and temporary strain softening for moist tamped and dry deposited samples. Similar results have been presented by Vaid and Sivathalayan (2007), Wood et al. (2008) and Yang et al. (2008). In some cases (e.g. Jefferies and Been 2006), it was found that the smaller strain data were affected by fabric, while the critical states were not. Shipton and Coop (2012) suggested that for the transitional soils different sample preparation methods seemed to have no significant effect other than through the different densities they created.

For tailings materials, Chang et al. (2011) investigated the effect of fabric on the mechanical behaviour of gold tailings through Scanning Electron Microscopy (SEM). Moist tamping produced an aggregated fabric while slurry deposition created a uniform fabric,

which was closer to that of in-situ samples. While the differences were strong for the coarsest tailings they tested, due to the presence of fine platy particles, for the medium and finest sized tailings, the effect of sample preparation was very small. Daliri et al. (2014) also showed influence of desiccation and rewetting on shear strength of tailings and found the desiccated samples appear to have a greater porosity, and also have greater face-to-face particle associations based on SEM images. It should be noted that the tailings tested by Daliri et al. (2014) contain many small particles, which are platy in shape, so the effect of desiccation might arise from the reorientation of those platy particles.

This work presented here mainly focuses on further investigating these issues. Iron tailings from Panzhihua were reconstituted with different preparation methods to assess the effects of fabric. Oedometer tests were conducted to identify whether non-convergent compression behaviour existed and to see what the effect of different gradings was. Then triaxial tests were carried out to check the uniqueness of the CSLs and to investigate the susceptibility to liquefaction.

METERIALS AND TESTING PROCEDURES

Materials

The Panzhihua iron tailings used in this study were taken from the surface layer within 50cm depth of three different locations on the tailings impoundment: the upper beach (UB), middle beach (MB), and pond (PO), as shown in Figure 1. The particle size distributions are shown in Figure 2. Due to faster sedimentation following discharge, sandy material formed the upper beach and the particle size changed gradually to a silty material in the pond. The particle sizes are slightly larger than those tested by Chang et al. (2011) for their gold tailings at similar locations, and the predominant change in the grading is a translation rather than a

major change to the uniformity, in contrast to what was assumed by Carrera et al. (2011) when they simulated the gradings change by adding increasing amounts of fines.

The specific gravity G_s of these three tailings was measured following ASTM D 854 (ASTM 2002), giving values of 3.365, 3.137, and 3.112 for UB, MB and PO respectively, which are relatively high mainly due to the presence of some metal minerals. The mineralogy of these iron tailings was investigated through X-ray diffraction (XRD) analysis. The parent rock was gabbro, which is a mafic intrusive rock. After extracting of the iron, the remaining parts are mainly consisted of pyroxene (diopside), feldspar (labradorite), hornblende, chlorite, and a small quantity of metal minerals like ilmenite and iron oxide. The minerals identified for the three gradings are quite similar, but with slightly changing in the quantities. The UB material, the coarsest one, contains more metal minerals, and the PO material, the finest one, contains more chlorite, which is a non-plastic clay-sized mineral. The liquid limits were determined by cone penetrometer method (BSI 1990), and because of the non-plasticity, the plastic limits were unavailable. SEM images were taken for the dispersed tailings particles to study the particle shapes. In this study, two particle shape descriptors, named the sphericity (S) and roundness (R) were quantified by visually observing the particles from the SEM images and using an empirical chart proposed by Krumbein and Sloss (1963). Table 1 shows details of the characteristics and major compositions for the three tailings. The relatively low S and R values indicate angular to sub-angular shapes of the tailings particles.

Oedometer testing

Oedometer and triaxial tests were conducted on the three tailings, as presented in Tables 2 and 3 respectively. For the oedometer tests, rings with diameters of 30mm and 50mm were used, each with a ring height of 20mm. The precise height of each oedometer sample was measured by several independent methods and an average value was taken as the sample

height. The maximum vertical stress applied to the sample was about 7MPa for the 50mm ring and 20MPa for the 30mm ring, the latter being of a floating ring type to minimize side friction while achieving higher stresses. Reconstituted samples were used since intact samples of these tailings were impossible to obtain as they collapsed even under a very small disturbance, due to inflow of water during excavation. Because of the difficulty to keep the process water, distilled water was used for all the tests.

Three different sample preparation methods were adopted: dry compaction, wet compaction and slurry, to investigate whether this would affect the behaviour. For the dry compaction method, the tailings were oven dried and then sprinkled gently into the oedometer ring from a constant height to achieve loose samples. A steel rod was used to compact the tailings with different number of impacts to obtain samples with different densities. For the wet compaction method, the tailings were compacted with 5-10% water content, using under-compaction (Ladd 1978). This method can create very loose and also dense samples, ensuring a larger range of densities. Generally, the samples were divided into three layers, and the first layer was compacted with less effort and the upper layer with greater effort in order to achieve a more uniform density of the sample along its longitudinal axis. For the slurry method, distilled water was added into the dry tailings gradually until the water content was close to or a little higher than the liquid limit. After that the mixtures were put into a vacuum desiccator to remove air, and then the prepared slurries were placed into the ring carefully to avoid air entrapment. Different density samples were produced by adding different amounts of water. The initial specific volumes of the slurry samples should probably represent better those that might be achieved in-situ, but the range of values that could be obtained was relatively small because for all initial water contents the specific volumes after applying initial seating loads and saturating tended to converge.

Triaxial testing

For the triaxial tests, most of the samples were tested using a Bishop and Wesley (1975) triaxial apparatus which can provide a maximum of 700kPa confining pressure. Some of them were tested using a high pressure triaxial apparatus which can provide a maximum of 7MPa confining pressure, to investigate the state boundary surface (SBS) of these tailings. The samples tested were 38mm in diameter and 76mm in height. Lubricated platens were used to minimize the friction at the end platens. Local linear variable differential transformers (LVDTs) were adopted to measure the local axial and radial strains, and derive the small strain stiffnesses. Three preparation methods: dry compaction, wet compaction and slurry were again adopted. During the saturation stage, carbon dioxide (CO_2) and de-aired water were used to flush the samples first, and then all samples were saturated under back pressure, typically of about 300kPa, until B values of at least 0.95 were achieved. After the saturation stage, the samples were isotropically compressed and then sheared under drained or undrained conditions. In the data analysis, a membrane correction was taken into account, but because of the relatively small particle sizes, the membrane penetration effect was not significant. The membrane stiffness correction expressions used in this study were those suggested by Fukushima and Tatsuoka (1984).

Calculation of initial specific volume

In the investigation of transitional behaviour, it is important to ensure that locations of the NCL and CSL in the specific volume : log mean stress, v : lnp', plane are accurate. Low accuracy may lead to an incorrect identification of transitional behaviour, simply because the data are scattered due to this error. The initial specific volumes v_i of the samples were calculated using four different methods given in Equations 1 to 4,

$$v_i = \frac{G_s \gamma_w}{\gamma_{di}} \tag{1}$$

$$v_i = \frac{G_s \gamma_w (1 + w_i)}{\gamma_{bi}} \tag{2}$$

$$v_i = \frac{G_s \gamma_w (1 + w_f)}{\gamma_{bf} (1 - \varepsilon_{vol})} \tag{3}$$

$$v_i = \frac{w_f G_s + 1}{1 - \varepsilon_{vol}} \tag{4}$$

where G_s is the specific gravity, γ_w is the unit weight of water; γ_{di} is the initial dry unit weight; γ_{bi} and γ_{bf} are the initial and final bulk unit weights respectively; w_i and w_f are the initial and final water content respectively and ε_{vol} is the volumetric strain. Among them, Equation 4 needs the sample to be fully saturated at the final stage of the test. An average of these values was obtained, and the difference between any one value and the mean was used to assess the accuracy of the test. Generally, tests with scatter of larger than ±0.02 were discarded.

COMPRESSION BEHAVIOUR

One-dimensional compression

The one-dimensional compression data are presented in Figure 3. Samples with different initial densities were created to identify non-convergent compression behaviour (e.g. Nocilla et al. 2006), which was generally not done in previous investigations. As shown in Figure 3(a), the compression curves of the PO material are convergent at about 1MPa, and a unique one-dimensional normal compression line (1D-NCL) can be easily identified. Different sample preparation methods give almost the same convergence, so it can be considered that the behaviour of the pond material is not significantly affected by the sample preparation method. For the MB material (Figure 3b), the compression curves give much slower convergence and they still do not identify a unique 1D-NCL at the end of the tests which reached a maximum of 7MPa vertical stress. In the floating ring oedometer tests, which gave a maximum of 20MPa, the compression curves are finally convergent and a unique 1D-NCL

can be identified. For a given density, no significant differences of behaviour could be observed from different preparation methods, and the fabric differences from initial densities can only be erased by very high pressures. For the UB material (Figure 3c), the compression curves show a similar behaviour of the MB, which do not converge at 7MPa but have finally converged at 20MPa. In the small floating ring oedometer it was not possible to achieve the same wide range of initial specific volumes as in the larger ring, and judging from the compression curves of the densest MB and UB samples at 7MPa, it is possible that these might still not quite reach the unique 1D-NCL at 20MPa, if they could have been created, but it is clear that the trend is one of slow convergence at very high stresses.

For each 1D-NCL, the compression index C_c and the intercept at 1kPa N_{1D} were calculated using the following equation.

$$v = N_{1D} - C_c \log \sigma'_v \tag{5}$$

The results are presented in Figure 4 and the relationship between compression indices and the fines contents is shown in Figure 5. It can be seen that the compression index decreases with the increasing fines content, mainly due to the void space being filled with fines. Chang et al. (2011) did not investigate the compression behaviour of their three tailings gradings, but the data differ from those of Carrera et al. (2011) where a minimum C_c was found at an intermediate fines content, although this might result from the artificial gradings they used.

Quantification of the convergence

Some methods have been proposed to quantify the convergence of the compression curves. Among them, the method using an m value to quantify the convergence (Ponzoni et al. 2014) was adopted in this study. As shown in Figure 6, the m value is defined as the gradient of the v_{20} : v_{6000} graph. For soils with fully convergent compression curves, m is equal to 0, and for soils with perfectly parallel compression curves, m equals 1.

Figure 7 shows m values for all the three tailings, but here based on the initial specific volume at 10kPa vertical stress (v_{10}) and that of at the maximum stresses reached (v_{final}), either 7MPa or 20MPa. It can be seen that the relationships between v_{10} and v_{final} are curved and the m values are not constant for the MB and UB materials at 7MPa, which is different from the original definition which depended on them being straight. At lower specific volumes, the m value is larger while as the specific volume increases, the m value reduces. It is because the initial fabric is more difficult to erase when the initial specific volume is low, since the soil experiences much smaller volumetric strains and much higher stresses are therefore needed to reach the 1D-NCL. At such a low specific volume, the compression curves tend to be parallel to each other and the m value will be close to 1. On the other hand, when the specific volume is high, the compression curves tend to converge more easily as the volumetric strains are larger and the m value will be close to 0. So for a given final stress, the m values will evolve from 1 to 0 with increasing specific volume. When the final stress reaches 20MPa, the m values all reach 0 as the compression curves have finally all converged.

Figure 8 gives a simple sketch of this phenomenon showing the evolution of m values. The curves at different stress levels cannot cross, so as was discussed above for the MB and UB materials, if even denser samples could have been created, they might not quite still have converged at 20MPa. From Figure 7 it can be estimated that the initial specific volume for this to occur would have to be less than about 1.6 for the MB and 1.5 for the UB.

These data show that it is important to evaluate convergence not at a fixed stress but using a stress level that varies with the material tested, and that even if these materials are not strictly transitional, the convergence of the compression data is very slow and so the depositional density would affect the in-situ volume significantly to far higher stresses than the materials would ever experience.

SHEARING BEHAVIOUR

Stress-strain data

As the stress-strain behaviours of the three tailings are quite similar, only the data of the UB material are presented in Figure 9. To see the pore water pressure resulting from the supressed volume change of soil and also eliminate the effect of the confining pressure, the effective stress path of the excess pore water pressure, ($\Delta u - \Delta p$) is normalised by the mean effective stress at the start of shearing, p'_0. For the undrained tests, the loosest sample (No.9) sheared from 50kPa p'_0 showed strong softening to almost zero deviatoric stress on Figure 9(b), while all the other samples showed phase transformation followed by dilative behaviour. The deviatoric stresses generally reach an initial knee at about 1%-3% axial strain, which is a quasi-steady state, with positive changes of pore water pressure up to this point. Because of the subsequent dilative behaviour, the pore water pressures begin to reduce and the deviatoric stresses increase again with the increase of axial strain. Three tests (No.1, No. 3 and No.4) labelled by dotted circles in Figure 9(c) show very strong dilative behaviour which causes very high negative pore water pressure and as it drops towards minus 100kPa, cavitation occurs in the drainage system, after which the deviatoric stresses becoming unreliable, and the true critical states of these tests are therefore difficult to identify.

For the drained tests, the stress-strain curves show post peak strain softening behaviour, with peak stresses occurring at about 15%-25% axial strains. It can be seen in Figure 9(d) that, except for the high pressure sample (No.14), the volumetric strains are initially contractive and become dilative with the increase of axial strains because all of them are on the dry side of the CSL with negative state parameters. A small hyperbolic extrapolation was used for these less stable curves to estimate the volumetric strains at the critical states more accurately.

Stress paths

The stress paths of the PO material are shown in Figure 10. It can be seen that the end points of these triaxial tests define a unique CSL in q : p' space and the gradient of this line M is 1.40 so angle of shearing resistance at critical state, φ'_{cs} is 34.6º. The very loose sample (No.2) of the PO material sheared from 50kPa p'_0 shows compressive behaviour initially, and then tends to be dilative at about 2% axial strain, which means that this pond material is not easily liquefied. The stress paths of the MB material are shown in Figure 11. A unique CSL with gradient M of 1.36 is identified (φ'_{cs} = 33.7º). For the UB material, although there is some scatter, a unique CSL can still be identified with an M of 1.41(φ'_{cs} = 34.8º), as shown in Figure 12. The stress paths of the three tests mentioned above (No.1, No.3 and No.4) are again labelled by dotted circles, which show a sudden inversion of direction because of the cavitation. The arrows indicate the directions of movement of these tests, which should travel along a Hvorslev surface.

The shapes of the undrained stress paths are different at low and high stress levels. At low stresses, the stress paths are more “C” shaped with a less well defined phase transformation (PT) point. However, at higher pressures the paths are more “S” shaped, and the PT point is well defined. As shown in Figure 13, the loosest sample (No.9) of the UB material sheared from 50kPa p'_0 reaches liquefaction, but the stress path shows a small inversion at the end of the test, which results from the lateral restraint of the membrane at high strains.

The φ'_{cs} of these three materials are very close, which indicates that the gradings do not affect the friction angle of the iron tailings much, which is probably due to the similar mineralogy and perhaps more importantly similar angular to sub-angular particle shapes of all the sizes. This is similar to the finding of Carrera et al. (2011) but contrasts with that of Chang et al. (2011) who found higher φ'_{cs} for their MB samples than the UB or PO.

Critical states

The isotropic compression and shearing paths from the triaxial tests are presented in Figure 14 together with the 1D-NCLs. Since the isotropic NCLs, cannot be identified even at the end of the isotropic compression to several MPa for the MB and UB materials, estimated isotropic NCLs are indicated for these. The difficulty of identifying unique isotropic NCLs again stems from the slow convergence in compression. The critical state points of the tests are highlighted, and for the tests that were slightly incomplete on the UB material, end points from hyperbolic extrapolation are given. Unique CSLs with different shapes can be identified for each tailing. The existence of unique critical states, with none of the slow convergence that was seen in compression means that it is easier to erase differences of fabric through shearing.

The CSL of the PO material is still a straight line even at a low p' levels, which shows similar behaviour to clays, even if this material is non-plastic. With the increase of particle size, from MB to UB materials, the CSLs tend to become more curved at lower stresses which is a typical behaviour of sands. At higher stresses, the CSLs tend to be parallel to the 1D-NCLs. This evolution of shape contrasts with Carrera et al. (2011) who found curved CSLs for all gradings, but this may again result from their artificial gradings. No CSLs were given by Chang et al. (2011) in the v : lnp' plane and so this evolution with location in the impoundment is an important new finding. It has implications for the susceptibility to liquefaction as is discussed below.

The model presented by Gudehus (1996), which is an exponential function, has been used to fit the curved CSLs

$$e_i = e_{i0} \exp\left[-\left(3p'/h_s\right)^n\right] \tag{6}$$

where e_i is the current void ratio; e_{i0} is the maximum void ratio; p' is the current mean effective stress; h_s is the granulate hardness and n is a constant exponent between 0.3 and 0.5.

The curvature of the CSLs generally indicates the onset of particle breakage (e.g. Konrad 1998). The particle size distributions of iron tailings samples sheared from stress levels of about 6MPa are given on Figure 2. There was only a small amount of particle breakage for the UB and MB materials and no particle breakage was observed for the PO material. Although the material with no breakage is that with a straight CSL, the very small amounts of breakage do tend to reinforce the conclusion of Carrera et al. (2011) that particle breakage is not a necessary feature of a curved CSL.

Normalised stress paths

The stress paths of the three tailings have been normalised by equivalent pressures on the CSLs, p'_{cs}, as shown in Figure 15. The definitions of p'_{cs} are given in Equations 7 and 8 for straight and curved CSLs respectively,

$$p'_{cs} = \exp\left(\frac{\Gamma - v_i}{\lambda}\right) \tag{7}$$

$$p'_{cs} = \frac{h_s}{3}\left(-\ln\frac{v_i - 1}{v_{i0} - 1}\right)^{\frac{1}{n}} \tag{8}$$

where λ and Γ are the gradient and the intercept at 1kPa of a straight CSL; v_i and v_{i0} are the current specific volume and the maximum specific volume, and h_s and n are constants of the model of Gudehus (1996). The q/p'_{cs} values were further divided by M to obtain CSLs that plot at the point (1, 1) for each tailing.

For the PO material, an SBS can be clearly identified, and the stress ratio between the isotropic NCL and CSL is about 2.7, which is similar to that of many clays. For the MB and UB materials, the normalization cannot work well for the curved part of the CSL, which will give a very large apparent SBS, since the p'_{cs} value for a liquefied sample is near 0. So only the straight part has been normalised to investigate the SBS. From the isotropic compression

data although the isotropic NCLs cannot easily be identified, several samples seem to be reaching the estimated ones, so tentative SBSs can be identified. The SBSs have stress ratios between the isotropic NCL and CSL of about 2.75 and 4 for the MB and UB respectively, tending towards the higher values typical of sands (Coop and Lee 1993). They also develop a peak on SBS on the wet side of the CSL ($p'/p'_{cs}>1$), which is another feature of sands. State boundaries have not previously been identified for tailings, but it seems that there is therefore an evolution from a SBS that looks more like one for clays for the finer PO material, even if it is non-plastic, to SBSs that look increasingly like those of sands as the grading becomes coarser from MB to UB.

Effect of fabric

As mentioned above, there are many examples of effects of the initial fabric of soils from different sample preparation methods at both smaller and larger strain levels. In this study, the behaviour of samples prepared by compaction (wet and dry compaction) and slurry methods was compared at different strain levels. Figure 16(a) shows the relationship between shear stiffness, G and the current mean effective stress during shearing, $p'_{current}$, at different shear strain levels of the UB samples. The G values were calculated from tangents to the deviator stress-shear strain curves (dividing the gradients by three). For an undrained test the shear and axial strains are the same, and for drained the shear strains were calculated using Equation 9,

$$\varepsilon_s = \frac{2}{3}\left(\varepsilon_a - \varepsilon_r\right) \tag{9}$$

where ε_a and ε_r are the axial and radial strains from the local LVDTs. Up to 0.1% shear strain, about 2500 data points defined the deviatoric stress-shear strain curve. The shear modulus was then calculated by using linear regression over a maximum of around 50 consecutive points, fewer being used at the beginning of the test where data were sparser. For all the tests,

the stiffness decreases with increasing shear strain, although there is some scatter, but there is no significant difference between the compacted and slurry samples. Figure 16(b) shows the stress paths of UB samples with similar initial densities and sheared from similar stresses. It can be seen that the stress paths of samples prepared by different methods exhibit similar phase transformation with dilative tails. The exact shapes are controlled by the initial densities and also the stresses the samples were sheared from, so that a slightly sharper phase transformation is seen for the compacted sample sheared at 200kPa compared with that of the slurry sample, which is compatible with the slightly looser initial state. The shear strength at PT point normalised with consolidation pressure versus void ratio for those dilative UB samples is shown in Figure 17, following the method proposed by Al-Tarhouni et al. (2011). It can be seen that the normalised strengths at PT points show a well-defined trend, also independent of different preparation methods. Figure 18 shows the CSLs of samples prepared by the two methods. It can be seen that, for each tailing, samples prepared with different methods all reach the same CSL.

In summary, the samples prepared by different methods show similar mechanical behaviour at small to medium strain levels, although small differences still can be seen in the in the lengths of the dilative tails. Since it is difficult to obtain samples with exactly the same initial density by different preparation methods, it is considered that the differences are possibly attributed to the slightly different initial densities. For the critical state, it is clear that the preparation method does not have any significant effect in the v : lnp' plane, indicating that the length of the dilative tail and the undrained shear strength must indeed be a function of the density.

SEM images were also taken to investigate the fabric of triaxial samples prepared by wet compaction and slurry methods. The SEM samples were initially prepared in the same manner as triaxial samples, but did not undergo consolidation and shearing stages. After that

all the samples were dipped into liquid nitrogen (-196 °C) to facilitate flash freezing. The samples were then put into a freeze dryer with cold temperature (-50°C) and vacuum (0.03kPa) to make the ice sublimate directly, in which the frozen samples were dried in a period of more than 48 hours (Ahmed et al. 1974; Delage et al. 1996). After the freeze drying, the samples were gently broken into small fragments to reveal the required undisturbed surface, and then the small fragment was carefully mounted on an aluminium plate with carbon tape for the SEM test. The images are shown in Figure 19. Yang et al. (2008) have shown that the anisotropy resulting from particle orientation may give different CSLs, while the particles of all the gradings of the iron tailings are mainly angular to sub-angular, and no obvious particle orientation could be seen, which could be one reason for the uniqueness of CSL in both q : p' and v : lnp' planes.

Chang et al. (2011) identified a strong difference between moist tamped and slurry samples for their coarser gold tailings, which came from the presence of fine platy particles. These dispersed uniformly around and in between the more bulky particles in the slurry sample and the bulky sand skeleton provided the primary support. In contrast, a “flocked” fabric was observed in the moist tamped samples and the bulky sand particles were bridged by the flocked fine particles resulting in larger pores and greater possibility of strain-softening behaviour. For the iron tailings in this study, little difference of fabric could be seen between the two preparation methods from the SEM images of the PO and MB materials (Figure 19a-d), which agrees with Chang et al. (2011) that the finer materials were less susceptible to fabric effects. For the UB samples, some effects may be seen. The sandy particles contact each other with the few silty particles dispersed around and in between them in the slurry sample, as shown in Figure 19(e) but a dispersed state was not obvious as in Chang et al. (2011). The fabric of the wet compacted UB sample is shown in Figure 19(f), in which the major contacts are still the sandy particles with flocked silty particles in between the sandy

particles. In both cases, the mechanical behaviour of the UB tailing might still be controlled by the sand skeleton but not a bridge consisting of flocked silty particles as found by Chang et al. (2011), and this could be another reason for the independence of the CSL of each iron tailing of the sample preparation method. The reason why wet compaction methods may give different fabrics should be studied further. One possible reason was the dynamic wet compaction adopted in this study that perhaps tended to create a more uniform fabric than the static wet compaction that Chang et al. (2011) used. Alternatively, the differences may simply be the result of the lack of platy particles here and the differences of mineralogy; the tailings of Chang et al. were 70-90% quartz, with smaller amounts of muscovite, pyrophyllite and illite.

Relative locations of the CSL and susceptibility to static liquefaction

As presented in many papers (e.g. Thevanayagam et al. 2002; Carrera et al. 2011), the relative locations of the CSL were controlled by the fines content of the sample, which is the percentage of particles smaller than 0.063mm in the whole mixture. A "transitional fines content" (TFC) may be defined, below which the CSLs moved downwards in the v : lnp' plane with increasing fines content and above which they moved upwards. The TFC was about 40% Thevanayagam et al. (2002) and 50% for Carrera et al. (2011), and for Fourie and Papageorgiou (2001) no change of the downwards movement of the CSL was observed with a fines content even of 60%.

The relative positions of CSL of iron tailings in this study showed only a slight translation upwards as the fines content increased (Figure 18), which seems in contrast to the above conclusions. The major change to the CSL was its change of shape from curved to straight. However, the gradings of iron tailings are original but not artificial, and as noted above the gradings tend to translate more than rotate, so the application of a framework based on TFC

might not be appropriate, this being typically used when fines are added to coarse material, as in Carrera et al.'s investigation of the Stava tailings. The fines content values therefore vary a lot, changing from 15% for the UB material to 62% for the MB material.

The location of the CSL is of key importance as it controls susceptibility to liquefaction. Carrera et al. (2011) and Bedin et al. (2012) showed that a curved CSL gives rise to a changing susceptibility to liquefaction as the stress level increases. When the initial state lies above the horizontal asymptote of the CSL in the v : lnp' plane, true static liquefaction must occur because the critical state is undefined in the v : lnp' plane. With an increase of the confining pressure, the initial state will lie below the horizontal asymptote, so even if there may still be significant strain softening because the distance between the NCL and CSL is large in this curved section of the CSL, a stable state is eventually reached. This strongly strain softening type of behaviour is often referred to as flow failure or flow instability (e.g. Sladen et al. 1985; Chu and Leong 2002). As the confining pressure increases further, the strain softening reduces markedly, and the CSL becomes steeper and lies closer to and parallel to the NCL.

The susceptibility to liquefaction therefore depends both on the location of the CSL in the v : lnp' plane and also the range of possible initial states that a given grading might have. The specific volume at the horizontal asymptote of the CSL is a limit above which liquefaction must occur. It is shown on Figure 20 as v_{liq} (liquefaction), together with v_{max} and v_{min} which are maximum and minimum specific volumes obtained from oedometer tests, to investigate the susceptibility of liquefaction of the three iron tailings. For the UB and MB materials, a small extrapolation of the CSL was adopted to get v_{liq}. For the PO material the CSL remains straight at even the lowest pressures that could be reached in the triaxial tests and so v_{liq} is simply taken at v=1kPa, i.e. Γ, since the undrained strength would necessarily be very small at this state. The maximum specific volume measured using ASTM D4254 (ASTM 2002) is

also shown as v_a (air pluviation). Since this method is not suitable for sands containing more than 10% of fines (<63μm), v_a is only treated as a reference here. To simulate the in-situ specific volume, a sedimentation method was used in which the material was allowed to sediment under gravity; this is labelled as v_w (water pluviation) in the figure.

The values of v_a are probably not a useful guide to likely in-situ densities and if they are disregarded, then the maximum and minimum specific volumes achieved in the oedometer tests may be taken as a range of possible states and this shows much less variability than was seen by Carrera et al. (2011). Also the movement of the CSL in the v : lnp' plane is much less here than they found. Based on the range v_{max} to v_{min}, the susceptibility to liquefaction reduces from UB to PO. For the PO material, containing 91% of fines, no liquefaction occurred even at a very loose state close to v_{max}. This is rather different from the findings of Carrera et al. (2011) who, based on a similar comparison, found that the material containing 100% silt showed a high risk of liquefaction. Carrera et al. (2011) did however reach a similar conclusion that their material containing 15% fines (similar to UB), is easier to be liquefied. The contrast of conclusions must again arise from the fact that for the actual in-situ gradings used in this study, the grading at any one location is relatively well graded, and not artificially graded with a variable fines content as investigated by Carrera et al. (2011). The present study is therefore likely to be more representative of real tailings. Chang et al. (2011) saw no full static liquefaction for any grading, only flow failure, but no data were presented in the volumetric plane. It can also be seen from Figure 20 that all the v_w points lie below v_{liq}, and since v_w, might be more representative of the likely in-situ volume, this would indicate that perhaps no grading might be expected to undergo full static liquefaction on shearing, although the proximity of v_w to v_{liq} would indicate that they might undergo severe strain softening or flow failure if they were severely disturbed. In reality, a number of techniques, such as de-watering or desiccation, have been used to increase the density of those very loose

sediments, which results in lower specific volume than the v_w, to improve their resistance to both static and cyclic loading.

CONCLUSIONS

A series of compression and shearing tests were carried out to characterise the mechanical behaviour of iron tailings obtained from Panzhihua City in China, within the context of critical state and recent transitional frameworks. Samples were taken from three different locations on the tailings impoundment; upper beach (UB), middle beach (MB), and pond (PO), giving a systematic investigation of the iron tailings with different gradings. The conclusions may be summarised as follows:

(a) The one-dimensional compression results show that unique 1D-NCLs can be identified for all the three iron tailings, and no transitional behaviour is observed. However, the rates of convergence from different initial densities to those lines are slow and are also variable, with the finest PO material reaching the 1D-NCL much earlier than the MB and UB materials. Different sample preparation methods gave very similar compression behaviour. The lower location of the line for the PO material and the higher initial specific volumes at which it may exist, mean that it reaches the 1D-NCL before the UB or MB materials.

(b) The m value presented by Ponzoni et al. (2014) was used to quantify the convergence of the compression curves. It is found that the relationship between v_{10} and v_{final} can be curved and the m values are not always constant, as previously assumed. For a given final stress, the m values will evolve from 1 to 0 gradually with increasing specific volume.

(c) Unique CSLs can be identified in q : p' space for all the three tailings, and the slopes of the CSLs are very close to each other, which indicates that the grading will not affect the friction angle of these materials much. Unique CSLs could also be identified at all stress levels in v : lnp' space, which are independent of the preparation method. The CSL of the PO

material remains straight even at low stress levels, similarly to clay soils. With the increase of particle size, from MB to UB, the CSLs tend to become more curved at lower stresses which is typical behaviour of sands. The SBSs also showed an evolution from more clay-like to more sand-like from PO to UB.

(d) Fabric studies revealed that, in contrast to the existing literature, the differences of fabric for different sample preparation methods are small in these tailings, so they have little effect on behaviour. This is not to say that this will generally be the case, as Chang et al. (2011) did show very clear fabric effects in the coarser tailing that they tested.

(e) The susceptibility to liquefaction depends on the location of the CSL in the volumetric plane as well as the range of possible states that the material may have. Both showed less variability than previously seen by Carrera et al. (2011). The liquefaction resistance of the three tailings tends to increase from the pond to the upper beach, which again contrasted with previous findings. The use of the actual in-situ gradings as opposed to artificial gradings with increasing fines content is likely to be the reason for this difference, since the actual gradings tend to translate in size rather than change their uniformity very much. The simulated in-situ specific volume, v_w, lies slightly below the v_{liq}, which indicates that these tailings might not undergo full static liquefaction in-situ bit that flow failure would be likely if they were severely disturbed for the UB and MB materials with curved CSLs.

ACKNOWLEDGEMENTS

The work described in this paper was fully supported by a grant from the Research Grants Council of the Hong Kong Special Administrative Region, China (project no. CityU 112813). Thanks go to Dr Li Xiongwei from Changzhou Institute of Technology, China, for his help in obtaining the tailings material. The authors also would like to acknowledge the anonymous

reviewers for their constructive comments and detailed suggestions that helped us to improve the quality of the manuscript.

NOTATION

1D-NCL one-dimensional normal compression line

C_c compression index

C_{cr} coefficient of curvature

CSL critical state line

C_u coefficient of uniformity

d_{50} mean particle size

e void ratio

G shear modulus

G_s specific gravity of soil particles

h_s granulate hardness

m gradient of v_{10} : v_{final} data

n material constant

N_{1D} intercept of one-dimensional normal compression line at 1kPa

p' mean effective stress

q deviatoric stress

q_{PT} shear strength at phase transformation point

R roundness

S sphericity

v specific volume

w_f final water content

w_i initial water content

w_L liquid limit

γ_{bf} final bulk unit weight

γ_{bi} initial bulk unit weight

γ_{di} initial dry unit weight

γ_w unit weight of water

Δu change of pore water pressure

ε_a axial strain from the local LVDTs

ε_r radial strain from the local LVDTs

ε_s shear strain

ε_{vol} volumetric strain

φ'_{cs} angle of shearing resistance at critical state

REFERENCES

Ahmed, S., Lovell, C.W., and Diamond, S. 1974. Pore sizes and strength of a compacted clay. Journal of Geotechnical Engineering Division, **100**(GT4): 407-425.

Al-Tarhouni, M., Simms, P., and Sivathayalan, S. 2011. Cyclic behaviour of reconstituted and desiccated-rewet thickened gold tailings in simple shear. Canadian Geotechnical Journal, **48**(7), 1044-1060.

ASTM 2002. Annual Book of ASTM standards.

Bedin, J., Schnaid, F., Da Fonseca, A.V., and Costa Filho, L. De M. 2012. Gold tailings liquefaction under critical state soil mechanics. Géotechnique, **62**(3), 263-267.

Been, K., and Jefferies, M.G. 1985. A state parameter for sands. Géotechnique, **35**(2), 99-112.

Been, K., Jefferies, M.G., and Hachey, J. 1991. The critical state of sands. Géotechnique, **41**(3), 365-381.

Bishop, A.W., and Wesley, L.D. 1975. A hydraulic triaxial apparatus for controlled stress path testing. Géotechnique, **25**(4), 657-670.

Bobei, D.C., Lo, S.R., Wanatowski, D., Gnanendran, C.T., and Rahman, M.M. 2009. Modified state parameter for characterizing static liquefaction of sand with fines. Canadian Geotechnical Journal, **46**(3), 281-295.

BSI 1990. BS1377: Methods of tests for soils for civil engineering purposes. BSI, London, UK.

Carrera, A., Coop, M.R., and Lancellotta, R. 2011. Influence of grading on the mechanical behaviour of Stava tailings. Géotechnique, **61**(11), 935-946.

Chandler R.J., and Tosatti G. 1995. The Stava tailings dams failure, Italy, July 1985. In Proceedings of the Institution of Civil Engineers - Geotechnical Engineering, 113, pp. 67-79.

Chang, N., Heymann, G., and Clayton, C. 2011. The effect of fabric on the behaviour of gold tailings. Géotechnique, **61**(3), 187-197.

Chu J., and Leong, W.K. 2002. Effect of fines on instability behaviour of loose sands. Géotechnique, **52**(10), 751-755.

Coop, M.R. 2015. Limitations of a Critical State Framework Applied to the Behaviour of Natural and "Transitional" Soils. In 6th International Symposium on Deformation Characteristics of Geomaterials, Buenos Aires, pp. 115-155.

Coop, M.R., and Lee, I.K. 1993. The behaviour of granular soils at elevated stresses. In Predictive soil mechanics (eds G. T. Houlsby and A. N. Schofield), Proceedings of the C. P. Wroth Memorial Symposium, London: Thomas Telford, pp. 186-198.

Daliri, F., Kim, H., Simms, P., and Sivathayalan, S. 2014. Impact of desiccation on monotonic and cyclic shear strength of thickened gold tailings. Journal of Geotechnical and Geoenvironmental Engineering, **140**(9), 04014048.

Davies, M.P., and Lighthall, P.C. 2001. Geotechnical Aspects of Several Recent Mine Tailings Impoundment Failures. In Proceedings of the 54th Canadian Geotechnical Society Conference, Calgary, Alta, pp. 321-326.

Delage, P., Audiguier, M., Cui, Y. J., and Howat, M. D. 1996. Microstructure of a compacted silt. Canadian Geotechnical Journal, **33**(1), 150-158.

Fourie, A.B., Blight, G.E. and Papageorgiou, G. 2001. Static liquefaction as a possible explanation for the Merriespruit tailings dam failure. Canadian Geotechnical Journal, **38**(4), 707-719.

Fourie, A.B., and Tshabalala, L. 2005. Initiation of static liquefaction and the role of K_0 consolidation. Canadian Geotechnical Journal, **42**(3), 892-906.

Gudehus, G. 1996. A comprehensive constitutive equation for granular materials. Soils and Foundations, **36**(1), 1-12.

International Commission on Large Dams (ICOLD) 2002. Tailings Dams - Risk of Dangerous Occurrences - Lessons Learnt from Past Experiences, Bulletin No. 121.

Ishihara, K. 1993. Liquefaction and flow failure during earthquakes. Géotechnique, **43**(3), 351-451.

Jefferies, M.G., and Been, K. 2006. Soil liquefaction – a critical state approach. Taylor & Francis, London & New York.

Konrad, J.M. 1998. Sand state from cone penetrometer tests: a framework considering grain crushing stress. Géotechnique, **48**(2), 201-215.

Krumbein, W.C., and Sloss, L.L. 1963. Stratigraphy and sedimentation. 2nd ed. San Francisco: Freeman and Company.

Ladd, R.S. 1978. Preparing test specimens using undercompaction. Geotechnical Testing Journal, **1**(1), 16-23.

Martins, F., Bressani, L.A., Coop, M.R., and Bica, V.D. 2001. Some aspects of the compressibility behaviour of a clayey sand. Canadian Geotechnical Journal, **38**(6), 1177-1186.

Nocilla, A., Coop, M.R., and Colleselli, F. 2006. The Mechanics of an Italian Silt; an Example of "Transitional" Behaviour. Géotechnique, **56**(4), 261-271.

Ponzoni, E., Nocilla, A., Coop, M.R., and Colleselli, F. 2014. Identification and quantification of transitional modes of behaviour in sediments of Venice lagoon. Géotechnique, **64**(9), 694-708.

Shipton, B., and Coop, M.R. 2012. On the compression behaviour of reconstituted soils. Soils and Foundations, **52**(4), 668-681.

Sladen J.A., D'Hollander R.D., and Krahn J. 1985. The liquefaction of sands: a collapse surface approach. Canadian Geotechnical Journal, **22**(4), 564-578.

Tan, C. K. 2004. Geotechnical properties & behaviour of tailings. Master's thesis, Imperial College London, UK.

Thevanayagam, S., Shenthan, T., Mohan, S., and Liang, J. 2002. Undrained fragility of clean sands, silty sands, and sandy silts. Journal of Geotechnical and Geoenvironmental Engineering, **128**(10), 849-859.

Vaid, Y.P., and Sivathayalan, S. 2007. Fundamental factors affecting liquefaction susceptibility of sands. Canadian Geotechnical Journal, **37** (3), 592-606.

Verdugo, R., and Ishihara, K. 1996. The steady state of sandy soils. Soils and Foundations, **36** (2), 81-91.

Vick, S.G. 1983. Planning, design, and analysis of tailings dams. New York: Wiley.

Wise Uranium Project (WISE) 2014. Chronology of Major Tailings Dam Failures [online]. Available from http://www.wise-uranium.org/mdaf.html.

Wood, F.M., Yamamuro, J.A., and Lade, P.V. 2008. Effect of depositional method on the undrained response of silty sand. Canadian Geotechnical Journal, **45** (11), 1525-1537.

Yamamuro, J.A., and Lade, P. V. 1998. Steady-state concepts and static liquefaction of silty sands. Journal of Geotechnical and Geoenvironmental Engineering, **124**(9), 868-877.

Yang, J. 2002. Non-uniqueness of flow liquefaction line for loose sand. Géotechnique, **52**(10), 757–760.

Yang, Z.X., Li, X.S., and Yang, J. 2008. Quantifying and modelling fabric anisotropy of granular soils. Géotechnique, **58**(4), 237-248.

Zlatovic, S., and Ishihara, K. 1997. Normalized behavior of very loose non-plastic soils: effects of fabric. Soils and Foundations, **37**(4), 47-56.

LIST OF TABLES

LIST OF FIGURES

Figure 9. Triaxial test data of the UB material: (a) stress-strain data; (b) expanded scale for the low p'_0 tests; (c) the relationship of change of pore water pressure with axial strain; (d) the relationship of volumetric strain with axial strain.

Figure 10. Stress paths and critical state line of the PO material: (a) all stress paths; (b) stress paths of tests at lower stress levels.

Figure 11. Stress paths and critical state line of the MB material: (a) all stress paths; (b) stress paths of tests at lower stress levels.

Figure 12. Stress paths and critical state line of the UB material: (a) all stress paths; (b) stress paths of tests at lower stress levels.

Figure 13. Stress path of a liquefied sample of UB material.

Figure 14. Critical state lines together with 1D-NCL & isotropic NCL in v : lnp' plane: (a) PO; (b) MB; (c) UB.

Figure 15. Normalised stress paths: (a) PO; (b) MB; (c) UB.

Figure 16. Fabric effect from different preparation methods on: (a) small strain stiffness; (b) stress path of the UB samples.

Figure 17. Shear strength at phase transformation (PT) point normalised with consolidation pressure versus void ratio for those dilative UB samples.

Figure 18. Fabric effect from different preparation methods on the critical state line.

Figure 19. SEM images of each material prepared by different methods: (a) slurry sample (PO); (b) wet compaction sample (PO); (c) slurry sample (MB); (d) wet compaction sample (MB); (e) slurry sample (UB); (f) wet compaction sample (UB).

Figure 20. Specific volumes of the samples at different states.

Table 1. Characteristics and compositions of the three tailings.

Tailings type	PO	MB	UB
d_{50} (mm)	0.023	0.035	0.220
C_u	6.7	10	10.4
C_{cr}	2.2	1.1	2.6
G_s	3.112	3.137	3.365
w_L (%)	25	25	20
S	0.66	0.58	0.66
R	0.34	0.34	0.30
Diopside (%)	28.3	46.1	30.2
Labradorite (%)	24.1	40.2	32.3
Hornblende (%)	21.5	5.5	11.3
Chlorite (%)	16.4	5.4	9.0

Note: d_{50} mean particle size. C_u and C_{cr} coefficient of uniformity and curvature. G_s specific gravity. w_L liquid limit. S and R sphericity and roundness.

Table 2. Summary of the one-dimensional compression tests.

Material	Test no.	Φ (mm)	Preparation method	w_i (%)	v_i	σ'_{vmax} (kPa)
PO	1	50	wet compaction	10.32	2.278	7100
	2	50		10.43	1.723	7100
	3	50	dry compaction	0.00	2.028	7100
	4	50		0.00	1.741	7100
	5	50	slurry	27.57	1.840	7100
	6	50		28.89	1.881	7100
	7	50		32.85	1.982	7100
MB	1	50	wet compaction	4.90	2.100	7100
	2	50		10.08	1.800	7100
	3	30		10.25	1.639	19800
	4	30		9.62	1.813	19800
	5	30		10.31	1.672	19800
	6	50	dry compaction	0.00	1.716	7100
	7	50		0.00	1.660	7100
	8	30		0.00	1.720	19800
	9	50	slurry	21.72	1.655	7100
	10	50		20.61	1.622	7100
	11	50		21.36	1.614	7100
UB	1	50	wet compaction	10.60	1.595	7100
	2	50		11.64	1.681	7100
	3	50		9.57	2.050	7100
	4	30		10.37	1.633	19800
	5	30		9.68	1.784	19800
	6	50	dry compaction	0.00	1.615	7100
	7	50		0.00	1.526	7100
	8	50		0.00	1.481	7100
	9	30		0.00	1.573	19800
	10	50	slurry	17.74	1.596	7100
	11	50		16.70	1.579	7100
	12	50		17.63	1.597	7100

Note: Φ diameter of sample. w_i and v_i initial water content and specific volume. σ'_{vmax} maximum vertical stress.

Table 3. Summary of the triaxial tests.

Material	Test No.	Shearing type	Preparation method	w_i (%)	v_i	p'_0 (kPa)
PO	1	CIU_HP	wet compaction	9.98	1.770	6000
	2	CIU	dry compaction	0.00	1.911	50
	3	CIU	slurry	30.00	1.783	50
	4	CID	dry compaction	0.00	1.969	200
	5	CID	dry compaction	0.00	1.835	100
	6	CID	dry compaction	0.00	1.799	400
	7	CIU	dry compaction	0.00	1.802	50
MB	1	CIU_HP	wet compaction	5.40	1.750	6000
	2	CIU	slurry	25.00	1.707	100
	3	CIU	wet compaction	4.91	1.838	50
	4	CID	dry compaction	0.00	1.715	100
	5	CID	wet compaction	5.11	1.774	400
	6	CID	wet compaction	4.63	1.866	50
	7	CID	wet compaction	5.07	1.671	400
	8	CID_HP	wet compaction	4.92	1.638	6000
UB	1	CIU	dry compaction	0.00	1.596	200
	2	CIU	dry compaction	0.00	1.657	100
	3	CIU	dry compaction	0.00	1.533	110
	4	CIU	dry compaction	0.00	1.547	400
	5	CIU_HP	dry compaction	0.00	1.617	6000
	6	CIU	slurry	25.00	1.627	60
	7	CIU	slurry	20.00	1.537	200
	8	CIU	dry compaction	0.00	1.716	50
	9	CIU	wet compaction	2.34	1.861	50
	10	CID	dry compaction	0.00	1.677	100
	11	CID	dry compaction	0.00	1.551	100
	12	CID	dry compaction	0.00	1.613	550
	13	CID	dry compaction	0.00	1.599	200
	14	CID_HP	wet compaction	4.87	1.687	6000

Note: CIU isotropically consolidated undrained test. CID isotropically consolidated drained test. HP test conducted with high pressure triaxial apparatus. v_i and w_i initial specific volume and water content. p'_0 mean effective stress before shearing.

(a)

(b)

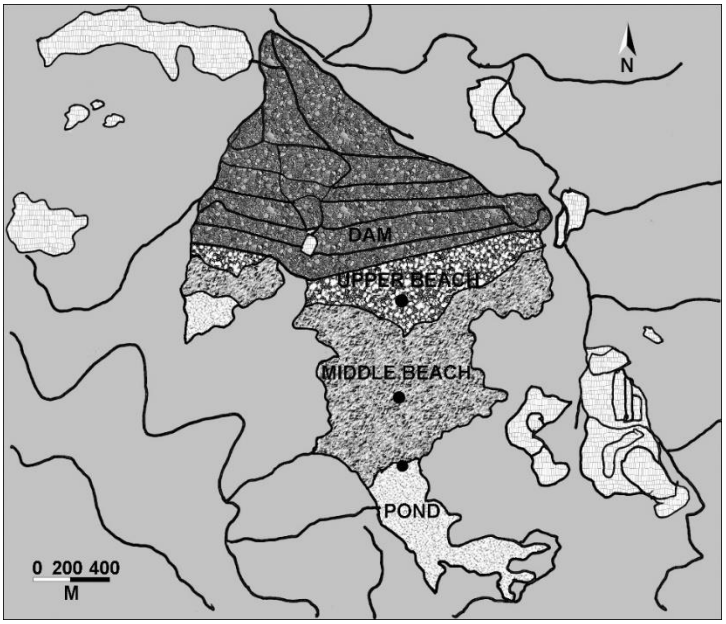

Figure 1. The tailings impoundment in Panzhihua City: (a) view of the tailings lagoon from the upper beach, (b) sketch of the tailings impoundment with sampling locations.

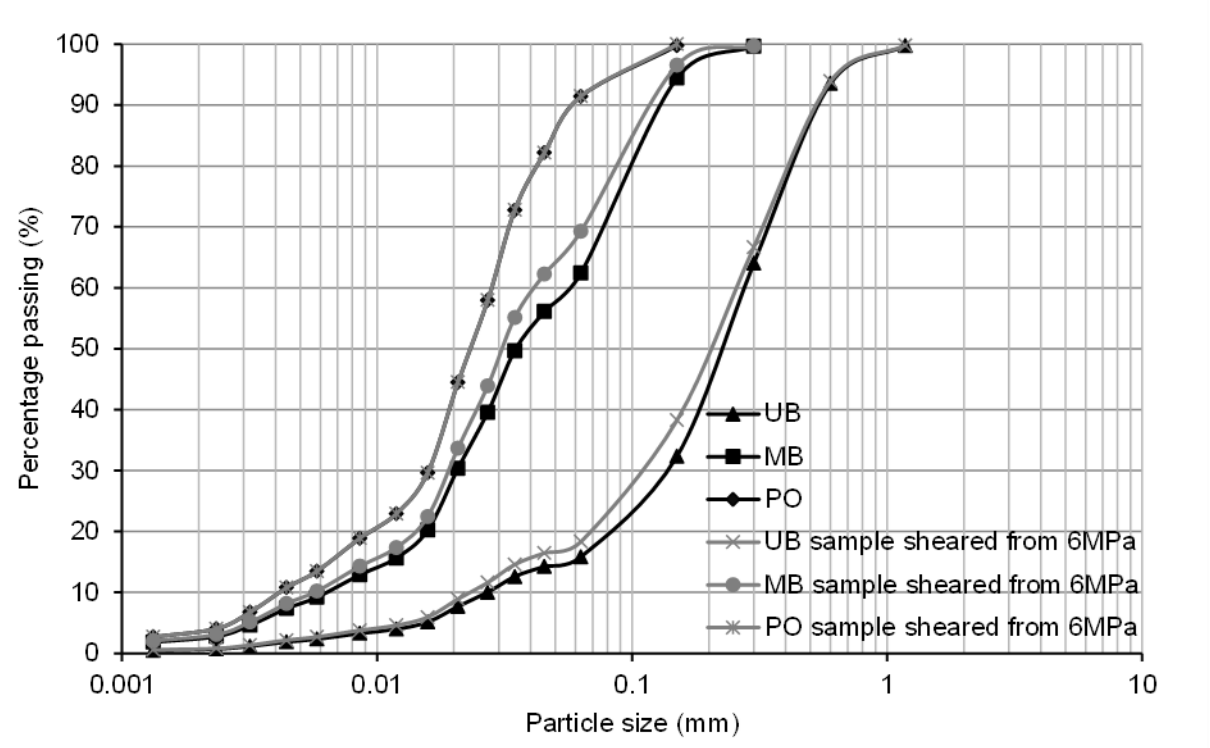

Figure 2. Particle size distributions of the tailings.

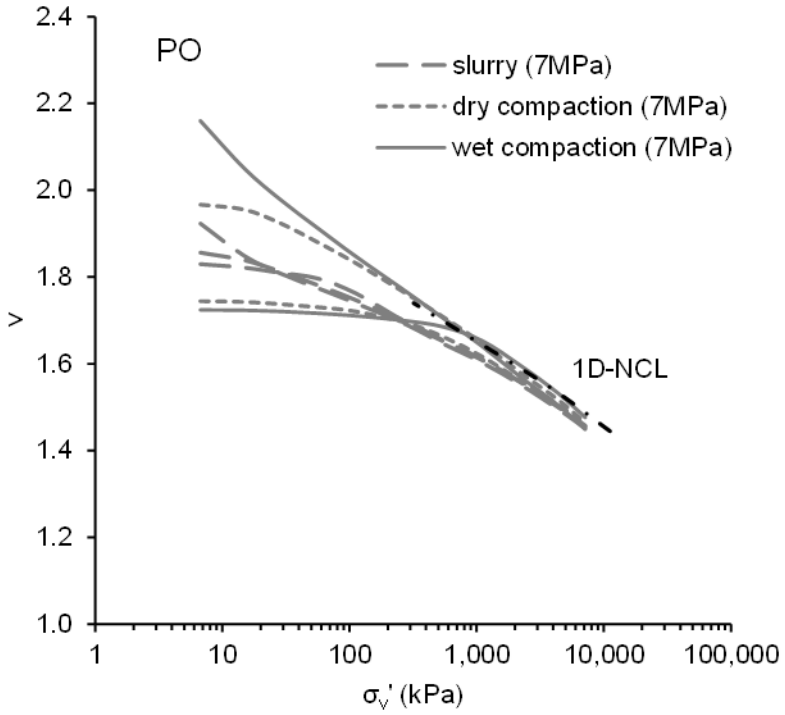

(a)

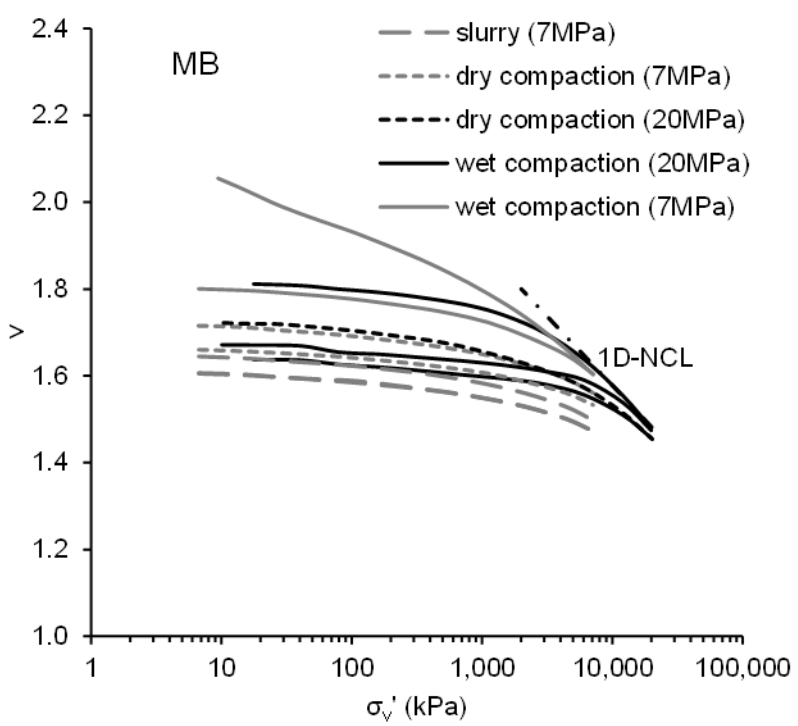

(b)

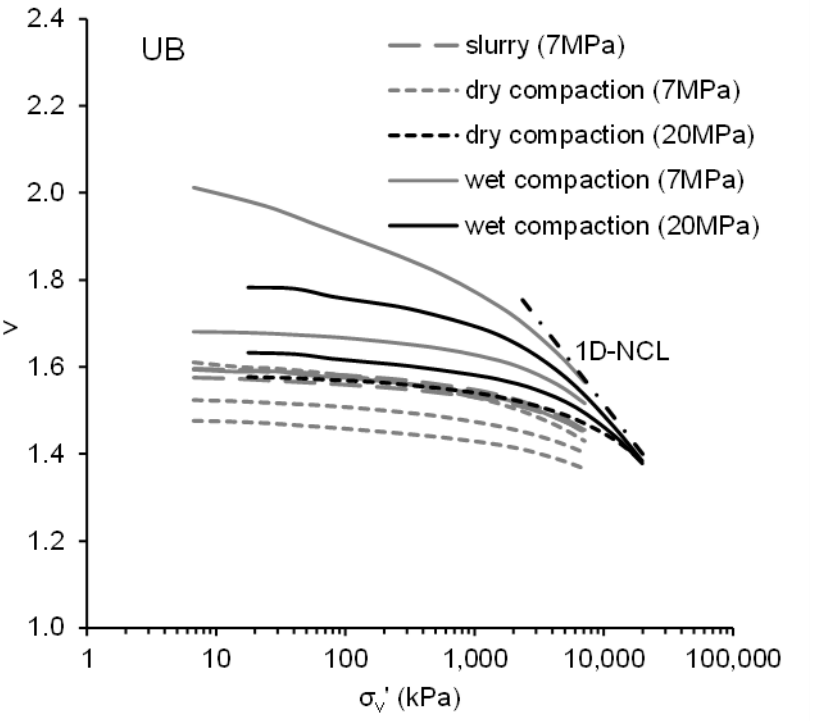

(c)

Figure 3. Compression curves from oedometer tests: (a) PO; (b) MB; (c) UB.

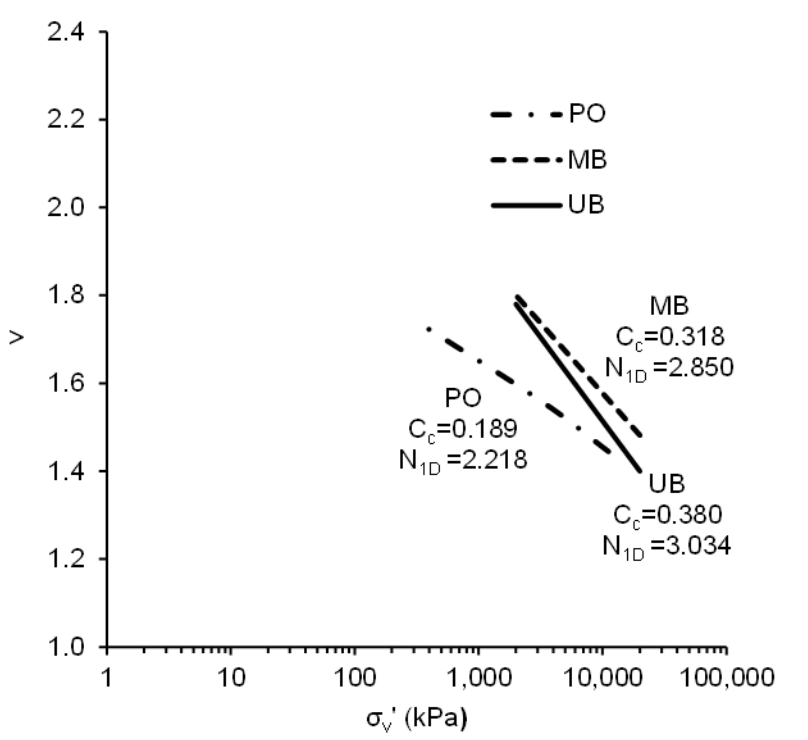

Figure 4. 1D-NCLs for the three tailings.

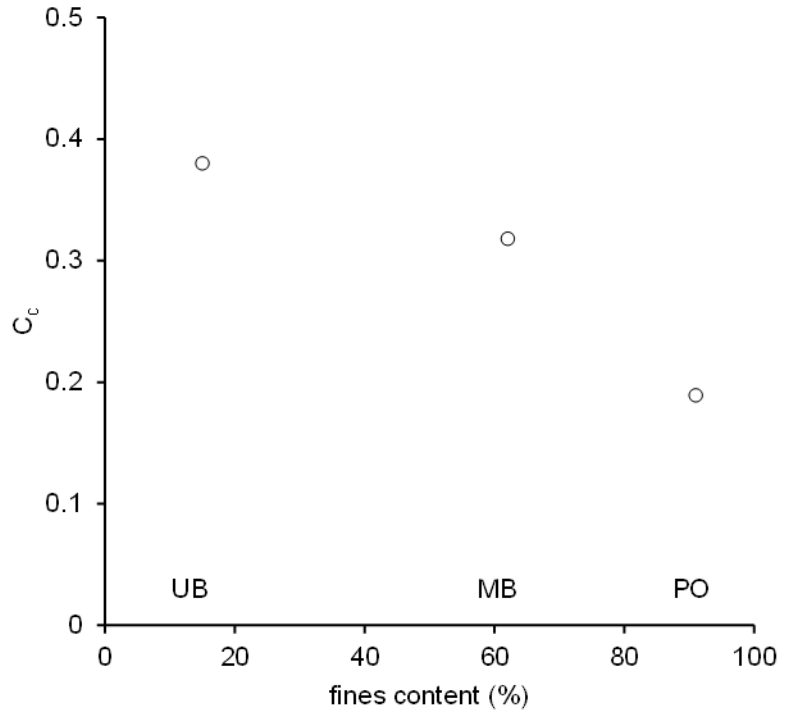

Figure 5. Relationship between fines content and compression index C_c.

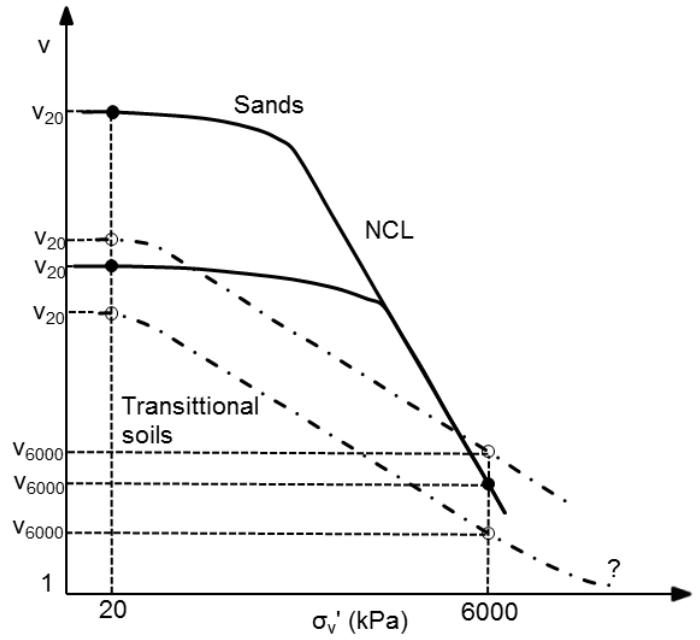

(a)

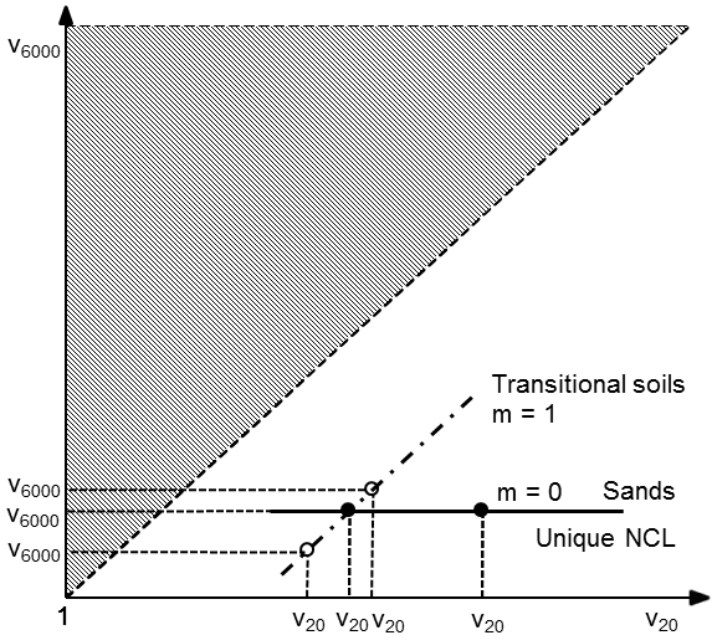

(b)

Figure 6. Quantification of the convergence of the compression curves (redrawn from Ponzoni, 2014): (a) schematic compression curves; (b) calculation of m.

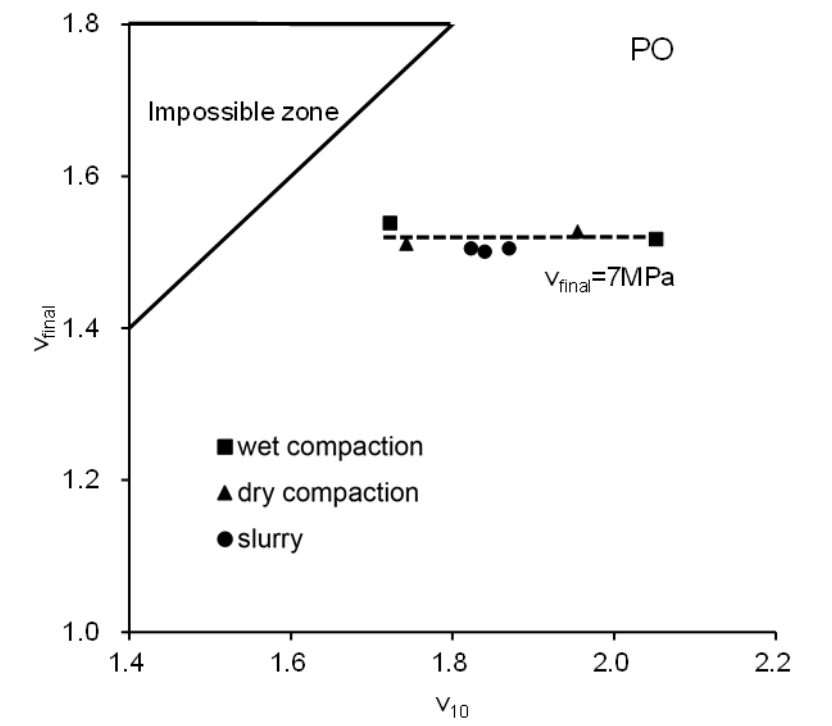
PO
Impossible zone
v_{final}=7MPa
wet compaction
dry compaction
slurry
v_{final}
v_{10}
1.8
1.6
1.4
1.2
1.0
1.4
1.6
1.8
2.0
2.2

(a)

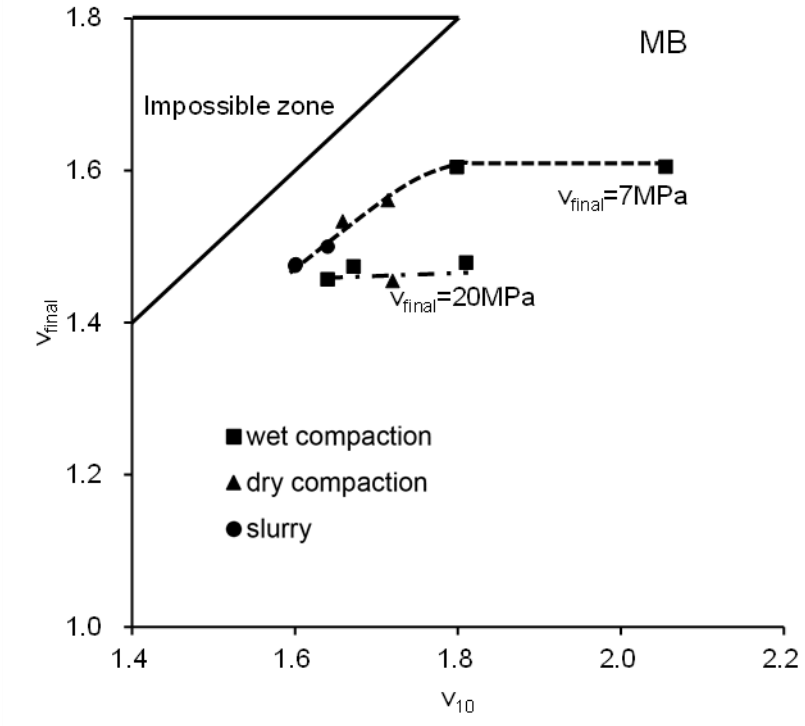
MB
Impossible zone
v_{final}=7MPa
v_{final}=20MPa
wet compaction
dry compaction
slurry
v_{final}
v_{10}
1.8
1.6
1.4
1.2
1.0
1.4
1.6
1.8
2.0
2.2

(b)

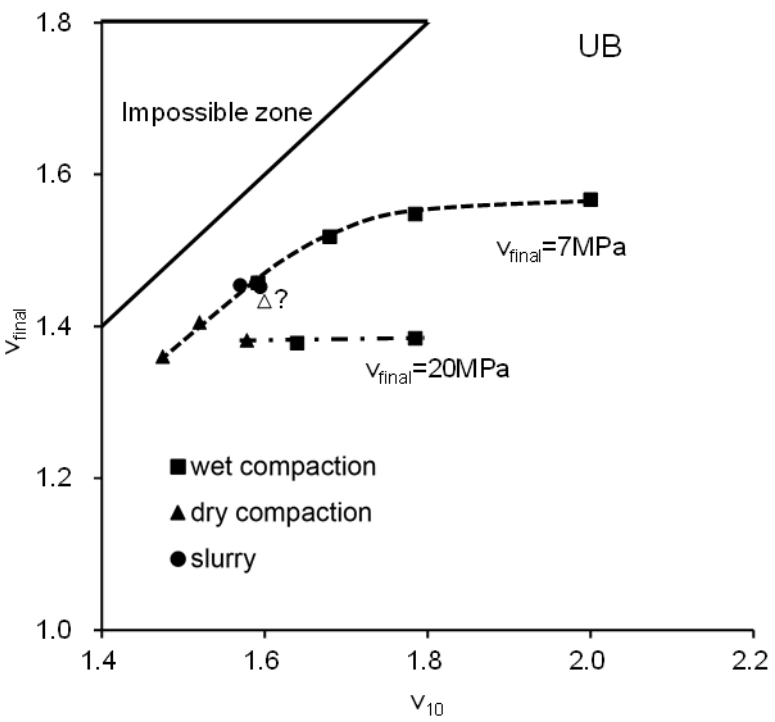

(c)

Figure 7. Evolution of m values with increasing v_{final}: (a) PO; (b) MB; (c) UB.

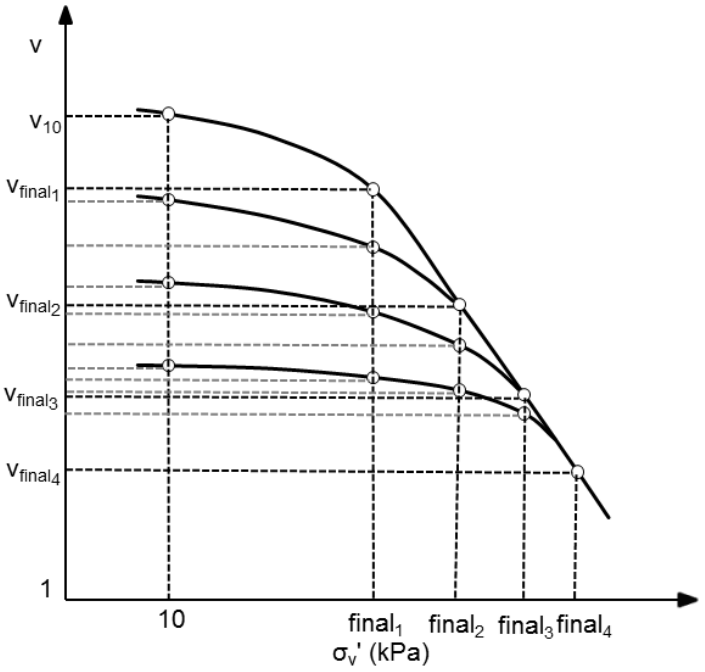

(a)

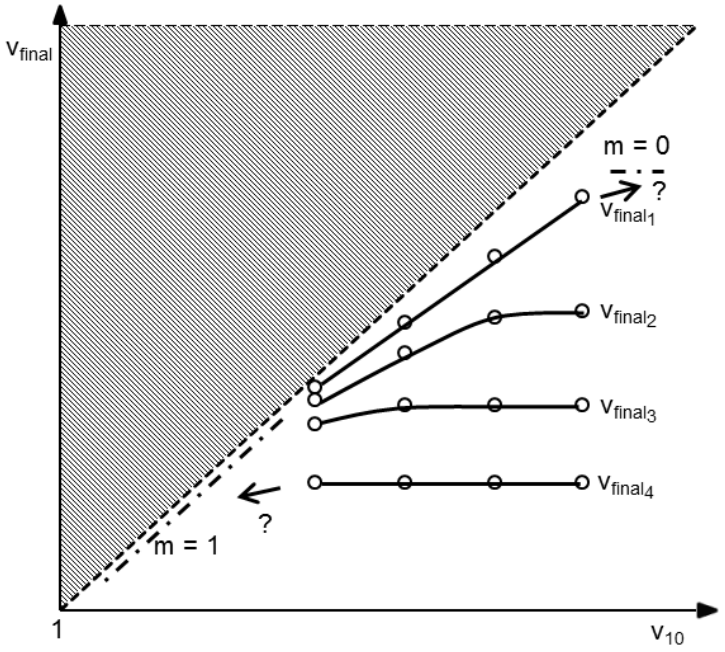

(b)

Figure 8. Evolution of m values with different specific volumes and stress levels (a) schematic compression curves; (b) evolution of m values.

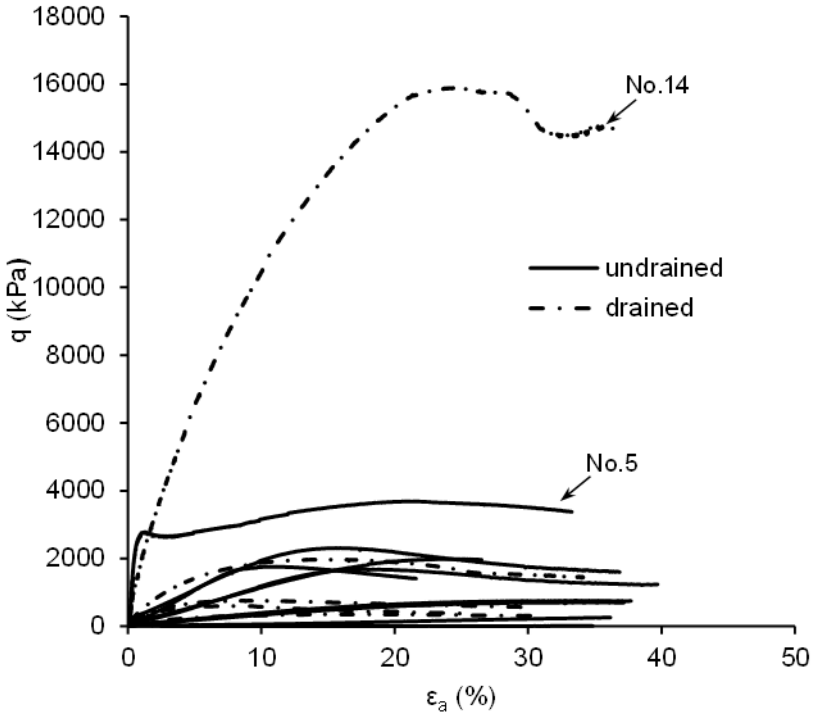

(a)

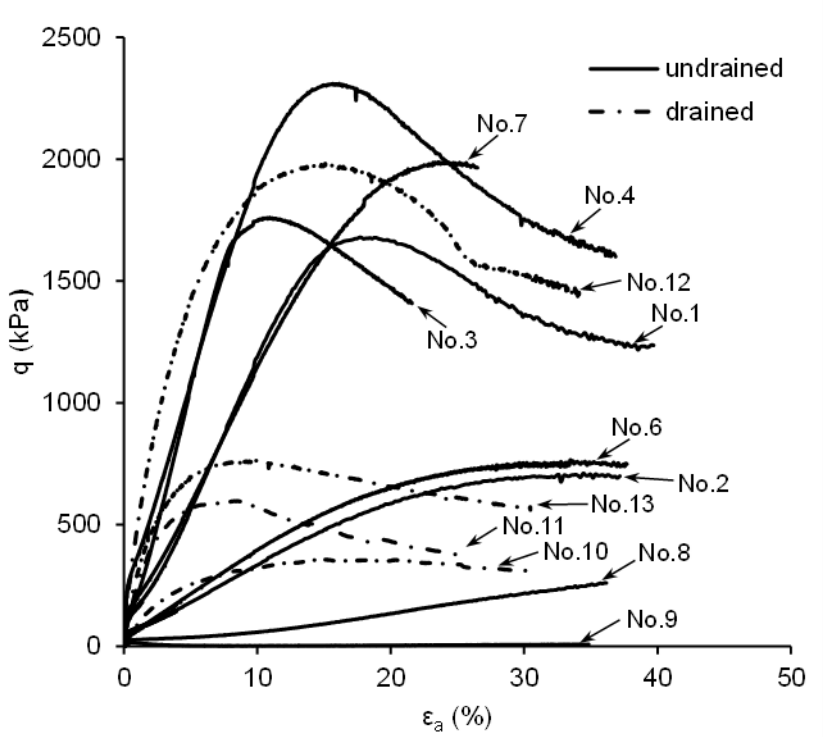
undrained
drained
No.7
No.4
No.12
No.1
No.3
No.6
No.2
No.13
No.11
No.10
No.8
No.9
q (kPa)
ε_a (%)

(b)

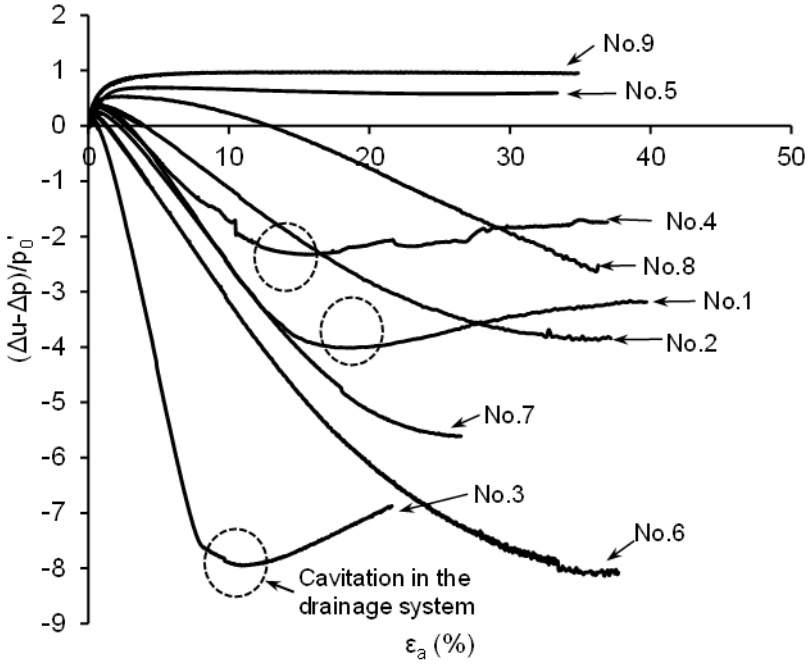
No.9
No.5
No.4
No.8
No.1
No.2
No.7
No.3
No.6
Cavitation in the
drainage system
$(\Delta u-\Delta p)/p_0'$
ε_a (%)

(c)

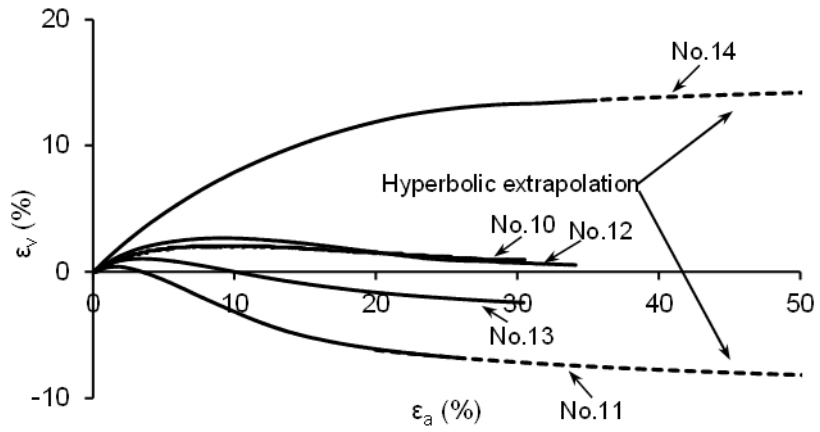

(d)

Figure 9. Triaxial test data of the UB material: (a) stress-strain data; (b) expanded scale for the low p'_0 tests; (c) the relationship of change of pore water pressure with axial strain; (d) the relationship of volumetric strain with axial strain.

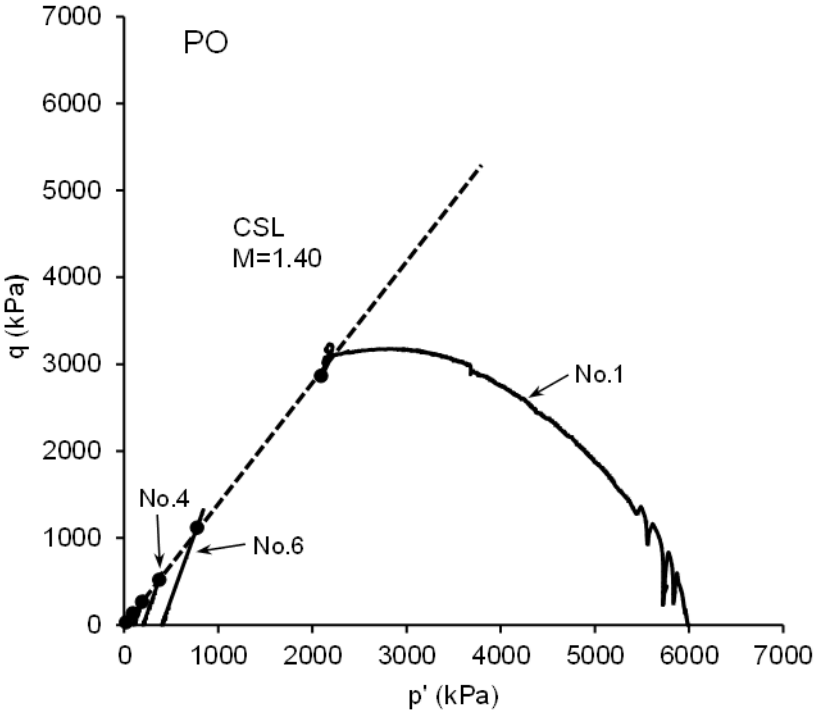

(a)

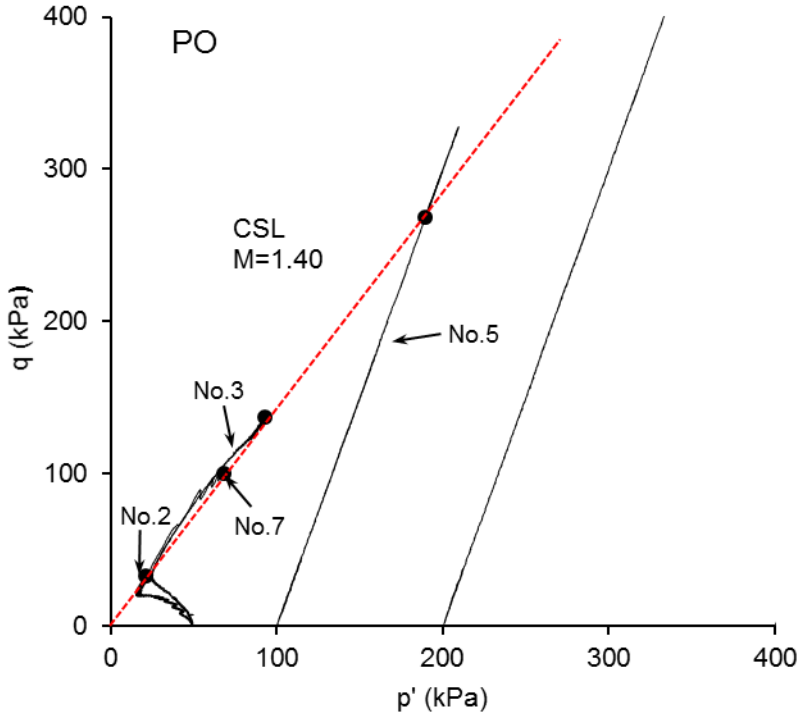

(b)

Figure 10. Stress paths and critical state line of the PO material: (a) all stress paths; (b) stress paths of tests at lower stress levels.

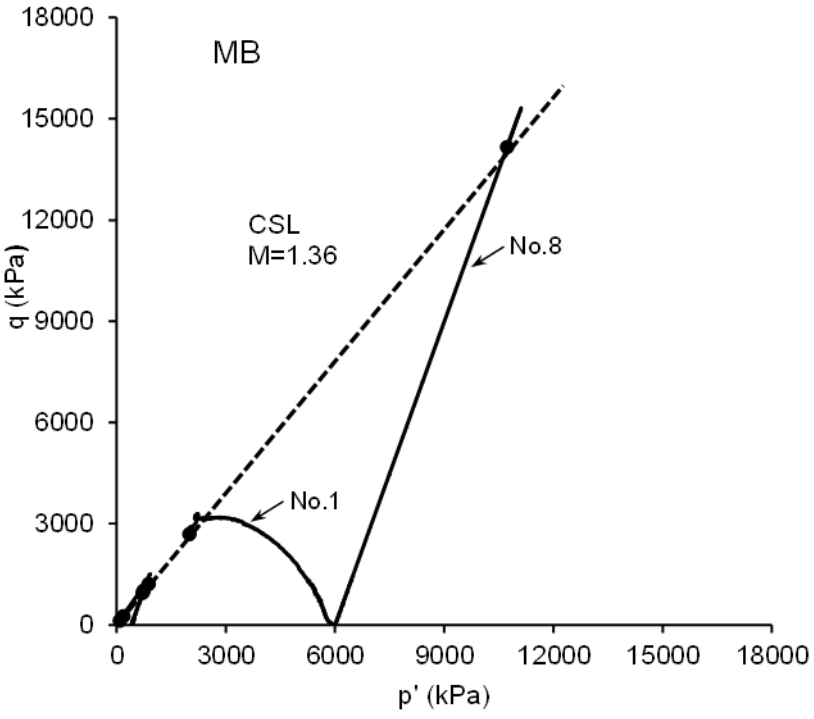

(a)

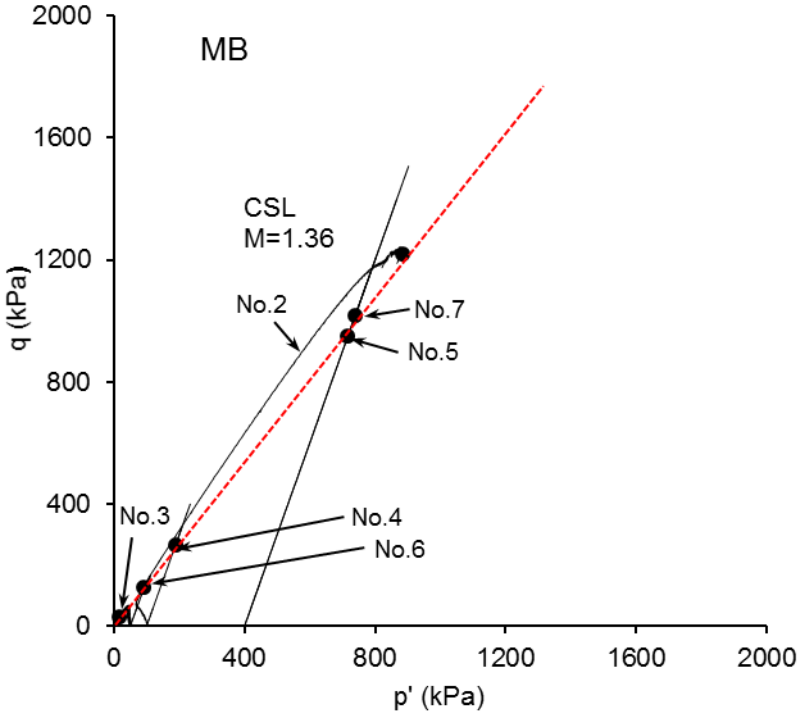

(b)

Figure 11. Stress paths and critical state line of the MB material: (a) all stress paths; (b) stress paths of tests at lower stress levels.

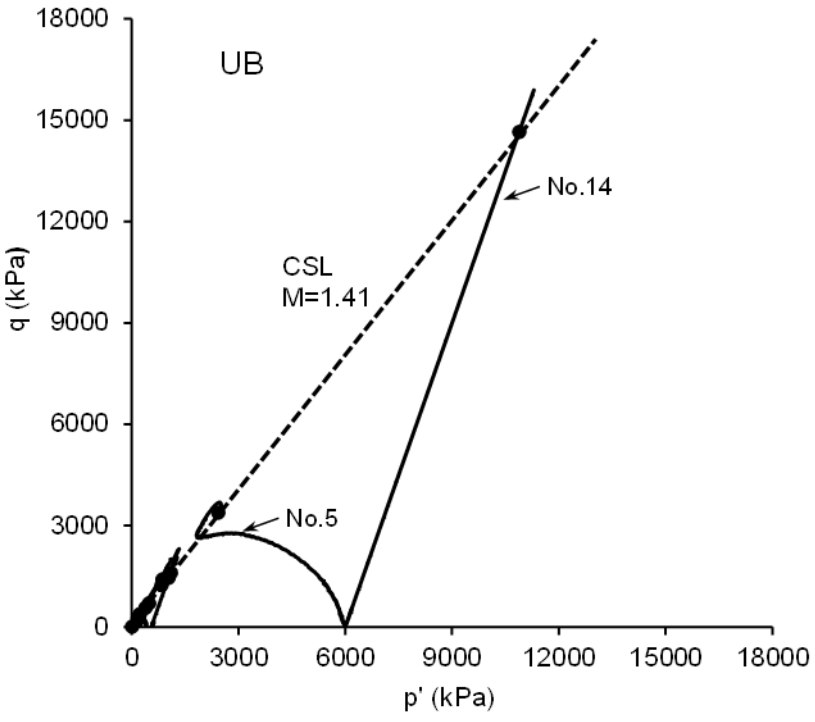

(a)

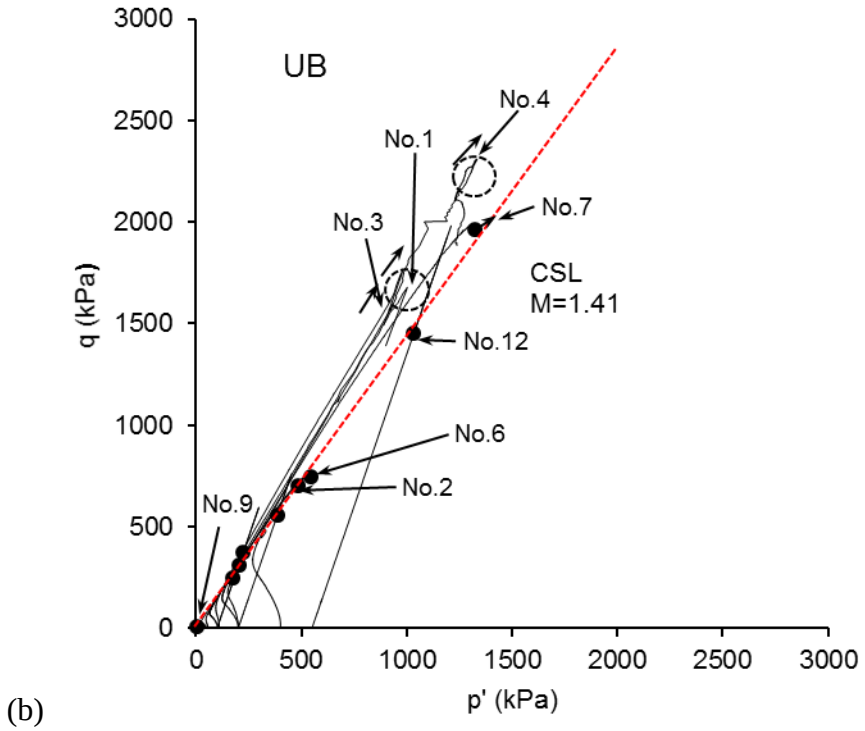

(b)

Figure 12. Stress paths and critical state line of the UB material: (a) all stress paths; (b) stress paths of tests at lower stress levels.

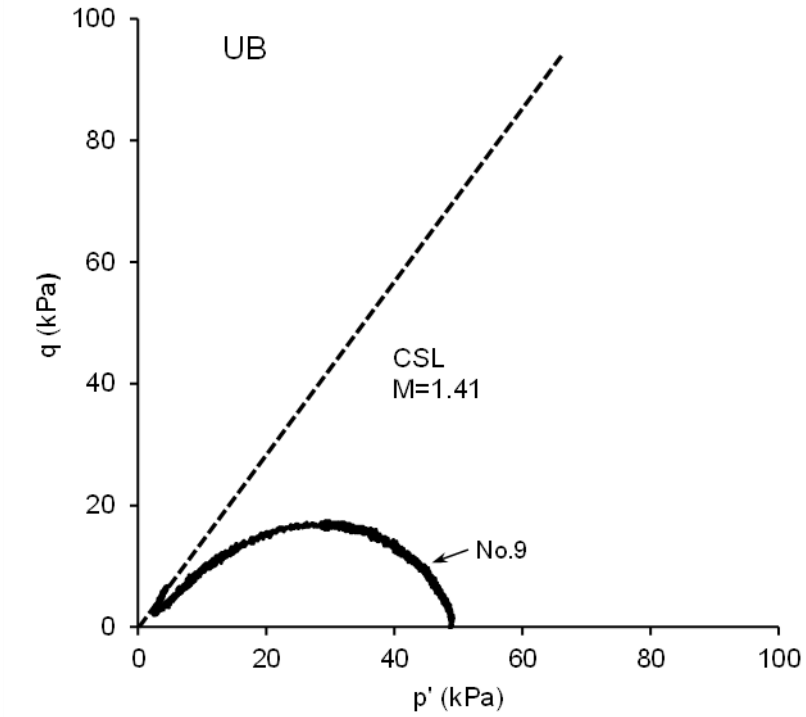

Figure 13. Stress path of a liquefied sample of UB material.

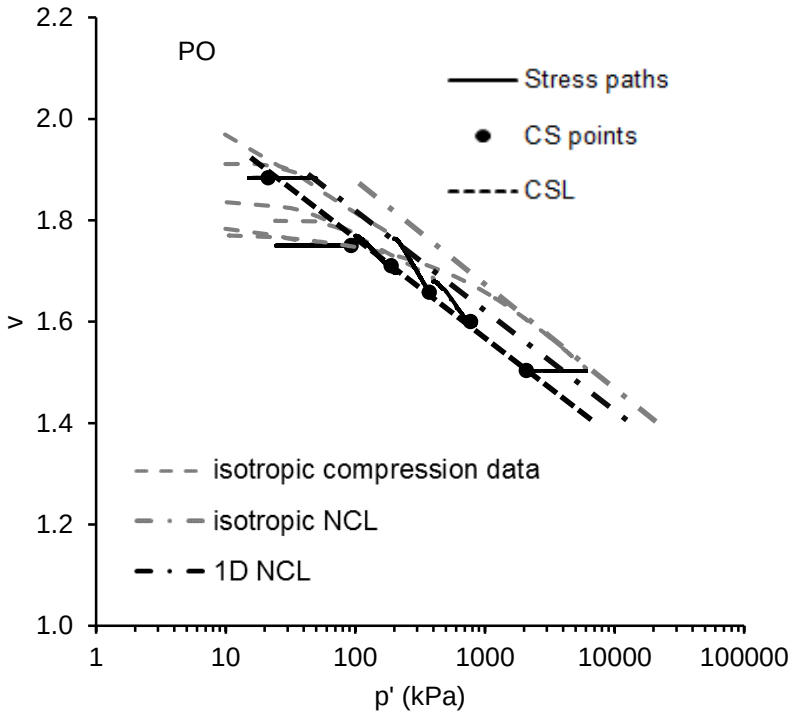
PO
Stress paths
CS points
CSL
isotropic compression data
isotropic NCL
1D NCL
v
p' (kPa)
2.2
2.0
1.8
1.6
1.4
1.2
1.0
1
10
100
1000
10000
100000

(a)

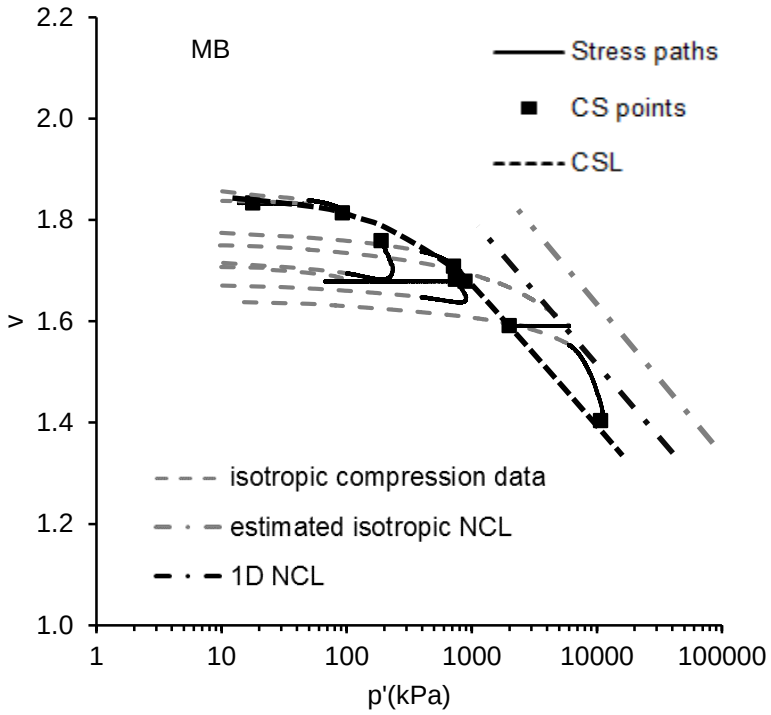
MB
Stress paths
CS points
CSL
isotropic compression data
estimated isotropic NCL
1D NCL
v
p'(kPa)
2.2
2.0
1.8
1.6
1.4
1.2
1.0
1
10
100
1000
10000
100000

(b)

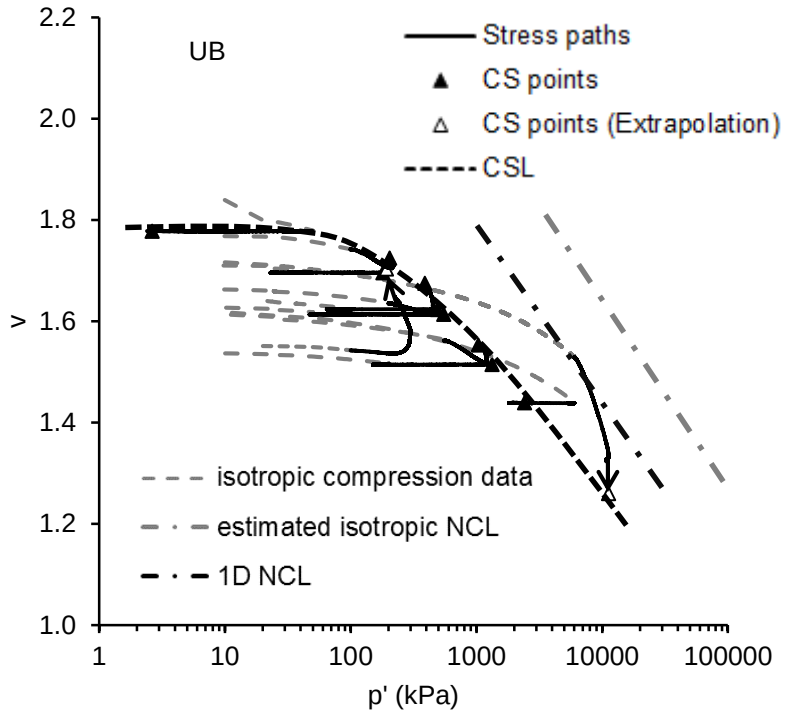

(c)

Figure 14. Critical state lines together with 1D-NCL & isotropic NCL in v : lnp' plane: (a) PO; (b) MB; (c) UB.

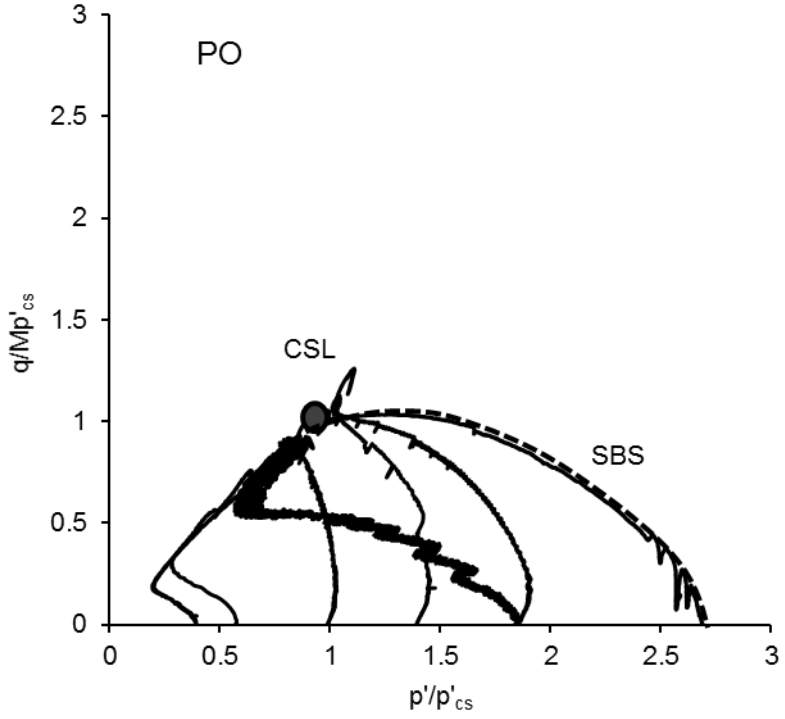

(a)

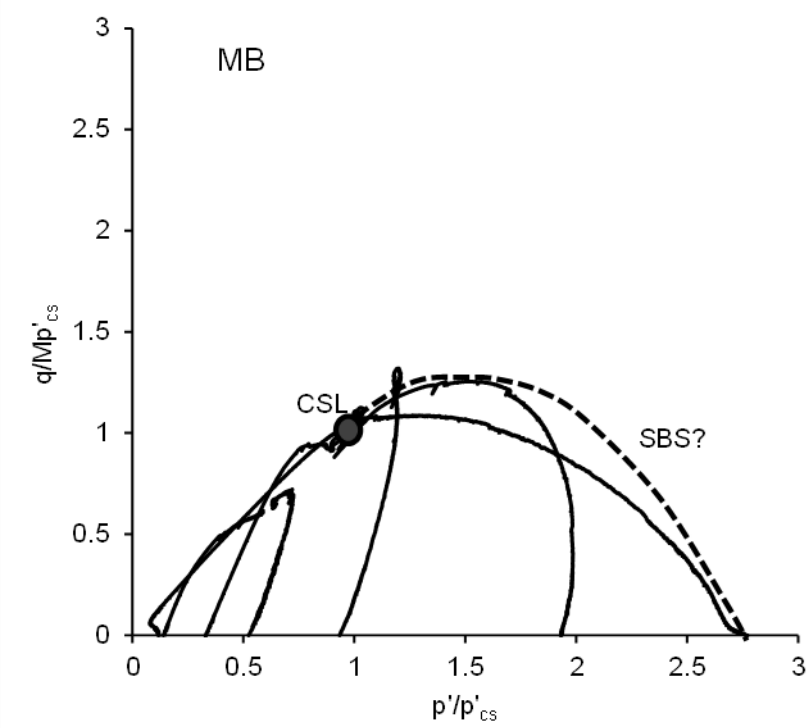

(b)

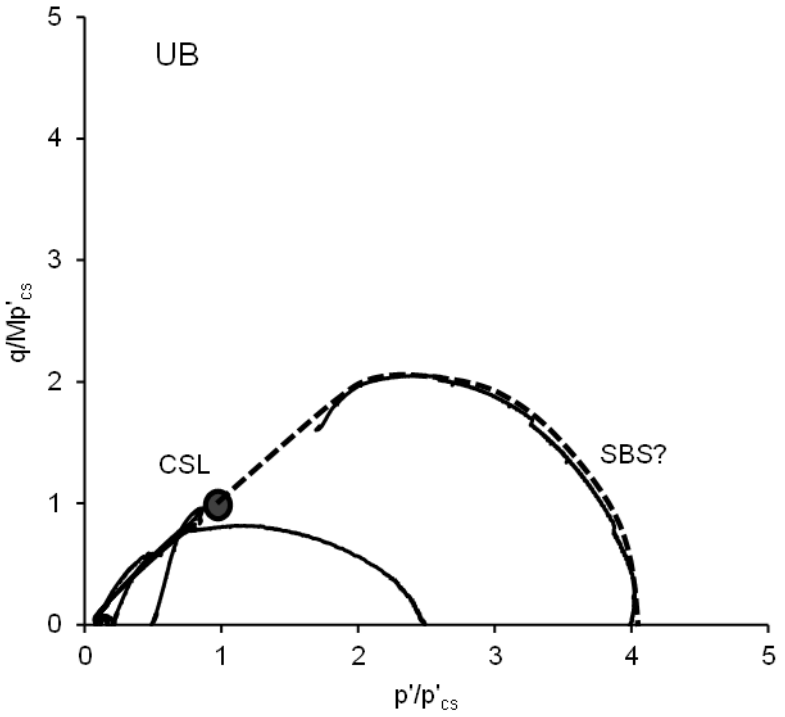

(c)

Figure 15. Normalised stress paths: (a) PO; (b) MB; (c) UB.

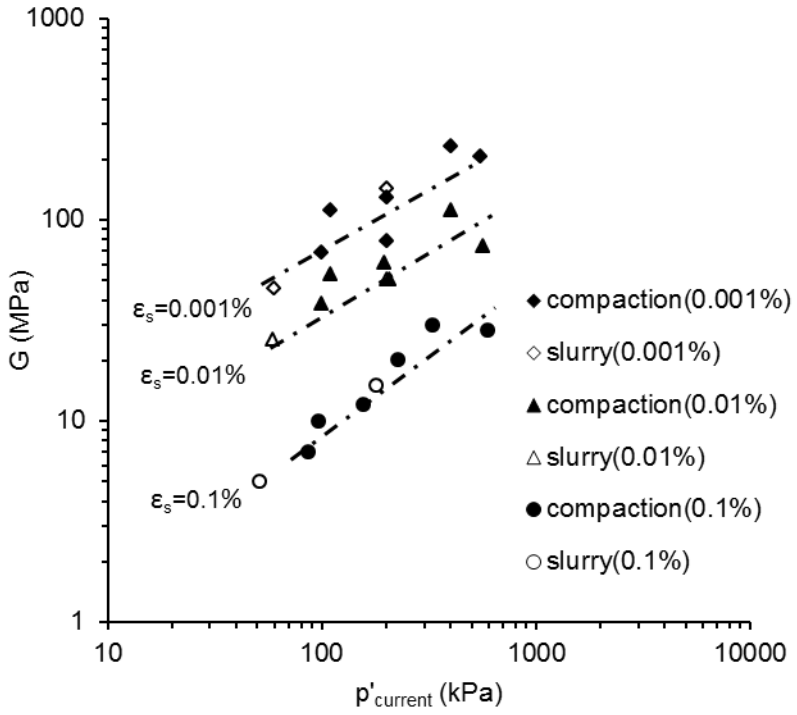

(a)

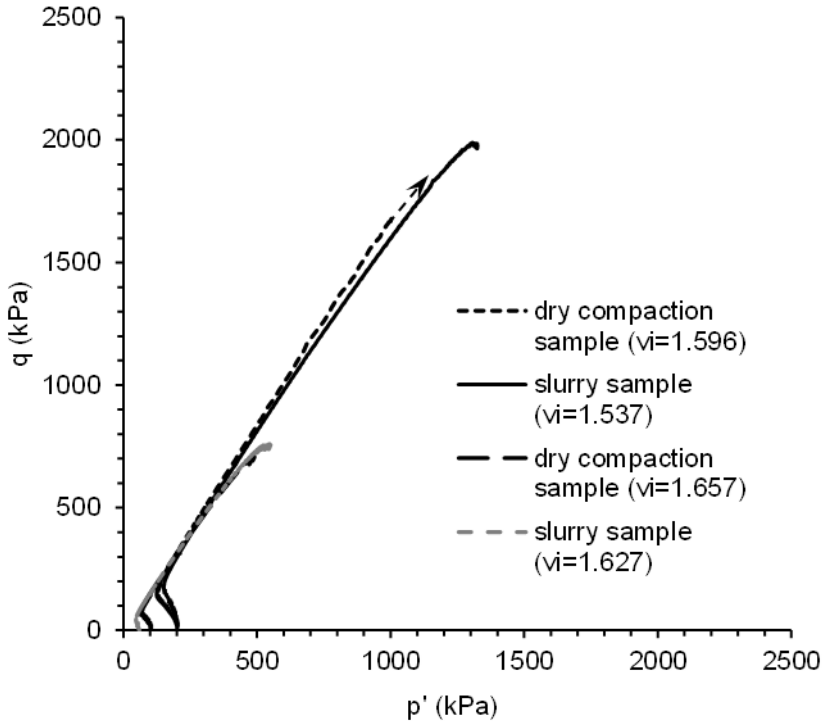

(b)

Figure 16. Fabric effect from different preparation methods on: (a) small strain stiffness; (b) stress path of the UB samples.

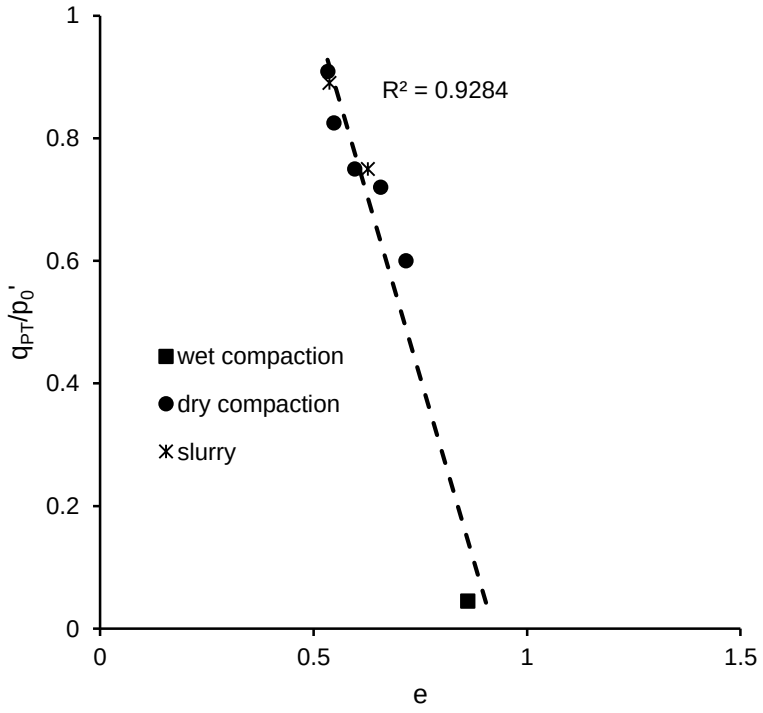

Figure 17. Shear strength at phase transformation (PT) point normalised with consolidation pressure versus void ratio for those dilative UB samples.

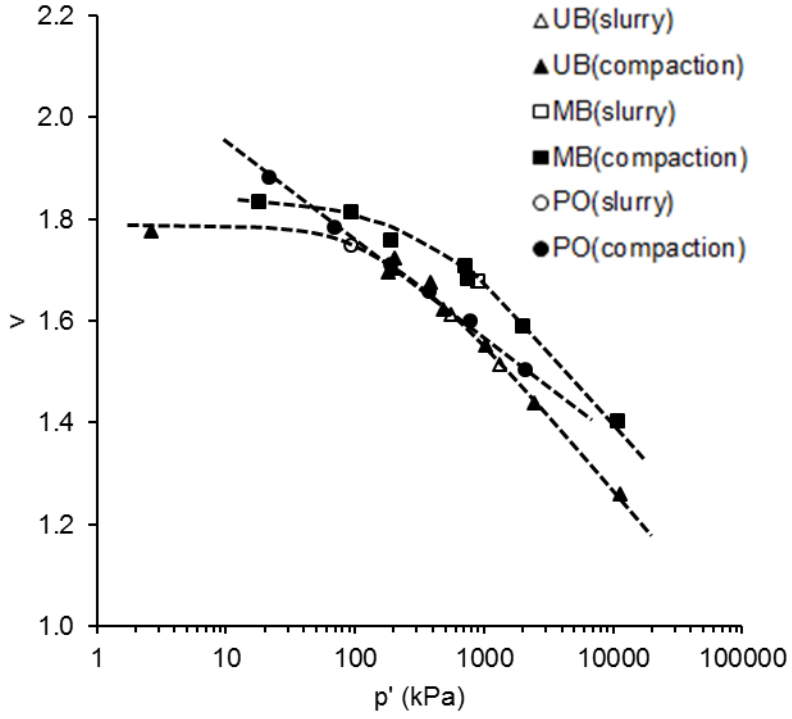

Figure 18. Fabric effect from different preparation methods on the critical state line.

(a)

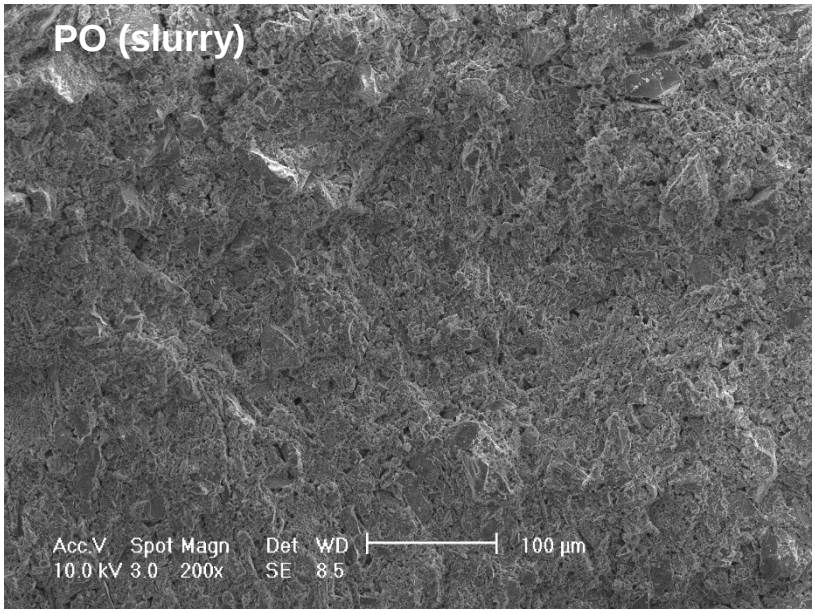
PO (slurry)
Acc.V Spot Magn Det WD 100 µm
10.0 kV 3.0 200x SE 8.5

(b)

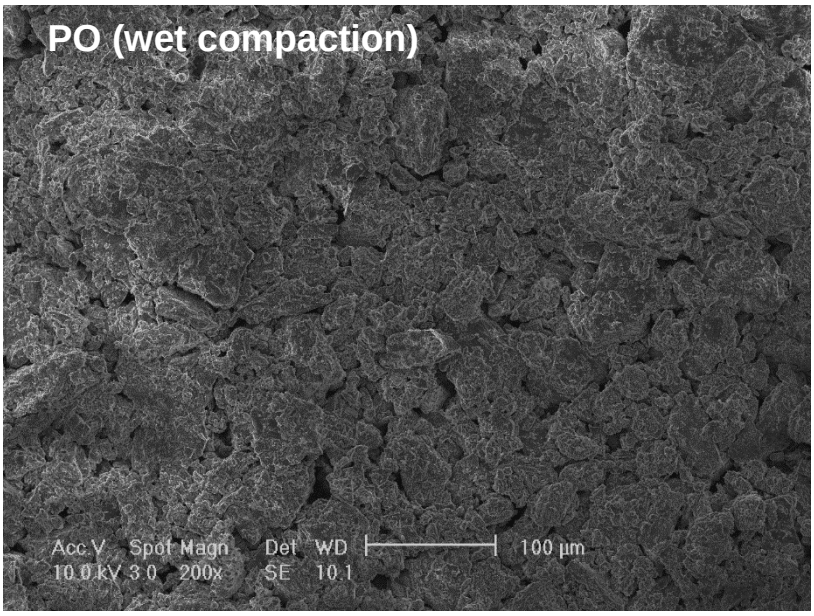
PO (wet compaction)
Acc.V Spot Magn Det WD 100 µm
10.0 kV 3.0 200x SE 10.1

(c)

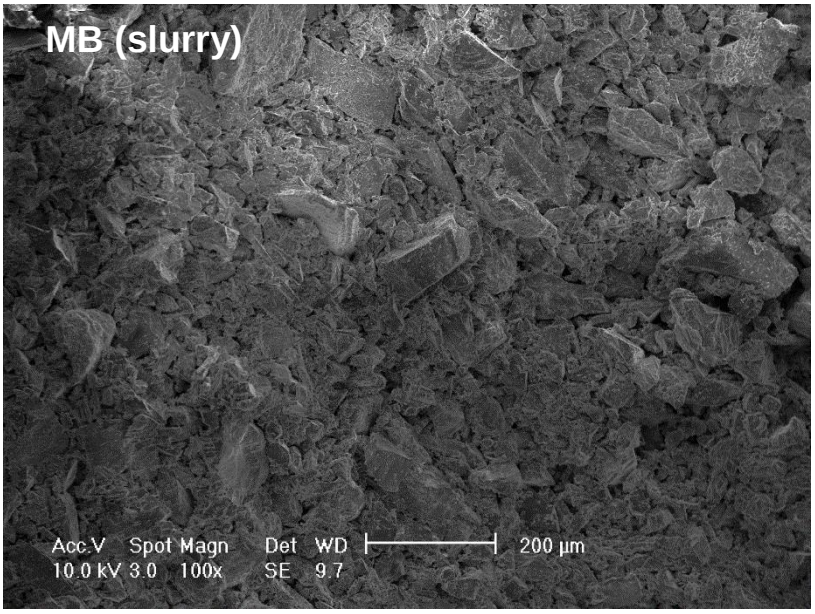
MB (slurry)
Acc.V Spot Magn Det WD 200 µm
10.0 kV 3.0 100x SE 9.7

(d)

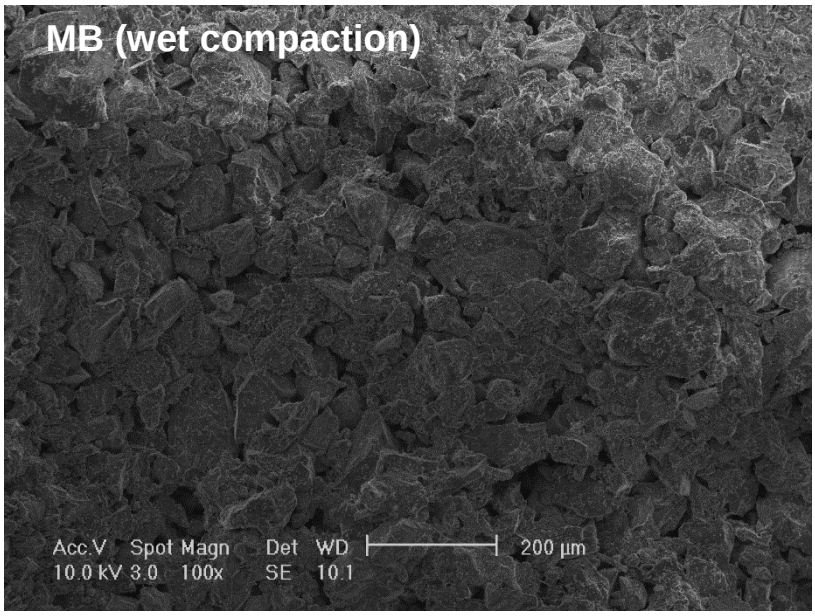
MB (wet compaction)
Acc.V Spot Magn Det WD 200 µm
10.0 kV 3.0 100x SE 10.1

(e)

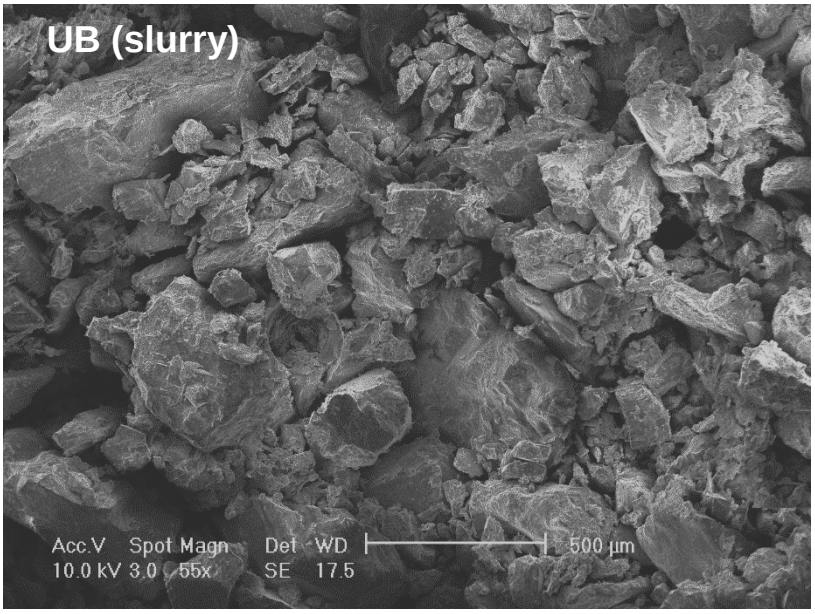

(f)

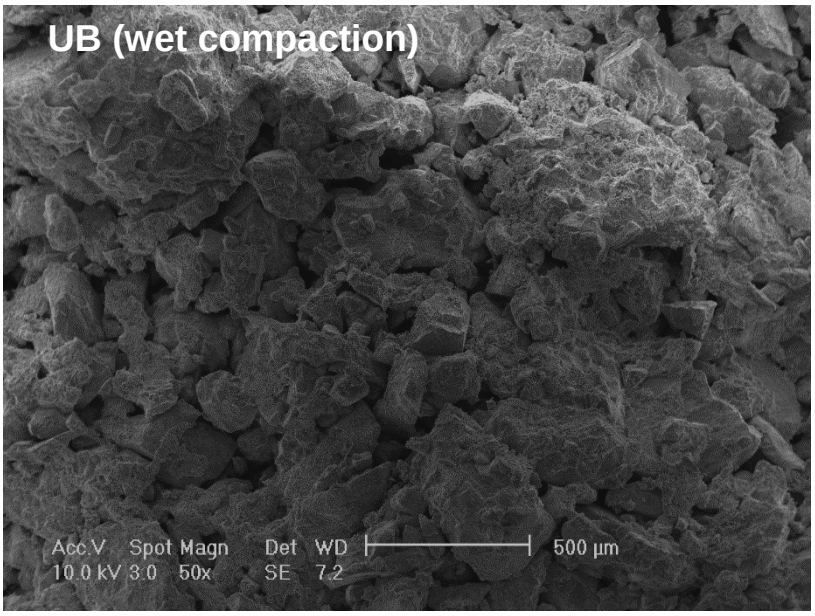

Figure 19. SEM images of each material prepared by different methods: (a) slurry sample (PO); (b) wet compaction sample (PO); (c) slurry sample (MB); (d) wet compaction sample (MB); (e) slurry sample (UB); (f) wet compaction sample (UB).

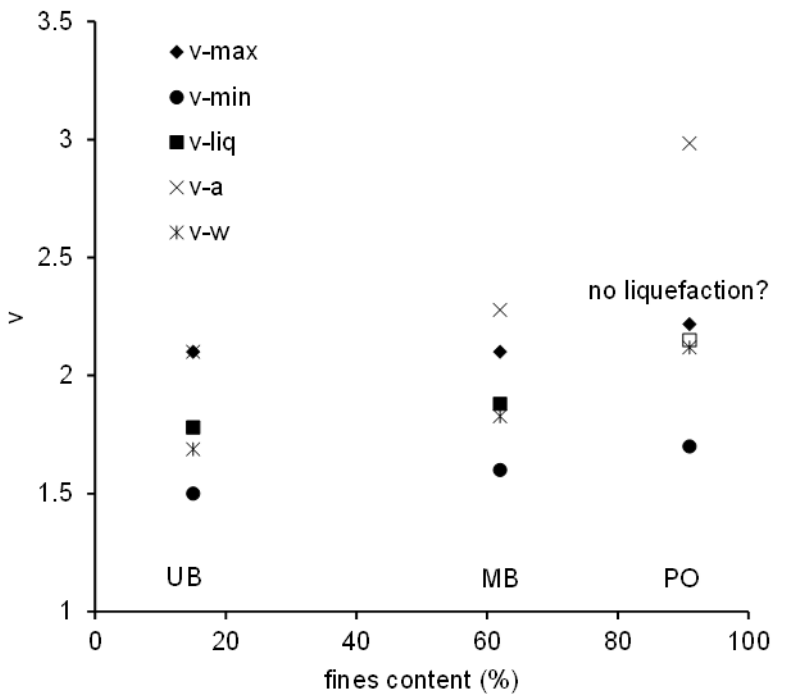

Figure 20. Specific volumes of the samples at different states.